Online Research @ Cardiff

information services
gwasanaethau gwybodaeth

Journal Pre-proof

Storm-induced hydrodynamic changes and seabed erosion in the littoral area of Yellow River Delta: A model-guided mechanism study

Yaoshen Fan, Shenliang Chen, Shunqi Pan, Shentang Dou

Please cite this article as: Fan, Y., Chen, S., Pan, S., Dou, S., Storm-induced hydrodynamic changes and seabed erosion in the littoral area of Yellow River Delta: A model-guided mechanism study, *Continental Shelf Research* (2020), doi: https://doi.org/10.1016/j.csr.2020.104171.

This is a PDF file of an article that has undergone enhancements after acceptance, such as the addition of a cover page and metadata, and formatting for readability, but it is not yet the definitive version of record. This version will undergo additional copyediting, typesetting and review before it is published in its final form, but we are providing this version to give early visibility of the article. Please note that, during the production process, errors may be discovered which could affect the content, and all legal disclaimers that apply to the journal pertain.

Storm-induced hydrodynamic changes and seabed erosion in the littoral area of Yellow River Delta: A model-guided mechanism study

Yaoshen Fan [a,c], Shenliang Chen [a,*], Shunqi Pan [b,a], Shentang Dou [c]

[a] *State Key Laboratory of Estuarine and Coastal Research, East China Normal University, Shanghai 200241, China;*

[b] *Hydro-environmental Research Centre, School of Engineering, Cardiff University, Cardiff CF24 3AA, UK;*

[c] *Yellow River Institute of Hydraulic Research, Yellow River Conservancy Commission, Zhengzhou 450003, China*

[*]Corresponding author.

Tel: 021-54836498; Email address: slchen@sklec.ecnu.edu.cn (S.L. Chen)

Highlights

- Storm-induced energetic hydrodynamic forces intensify sediment resuspension and dispersal significantly.

- Wave-induced bottom stress promotes sediment plume and enhances local resuspension.

- Storms increase suspended sediment concentration and offshore sediment transport.

- Storm-induced accumulative effect on seabed scour tends to cause long-term erosion.

22 **Abstract**

23   Morphological evolution of large river deltas is highly vulnerable to extreme

24 storm events due to insufficient sediment supply. As an abandoned delta lobe, the

25 coasts along the northern Yellow River Delta (YRD) and Gudong Oil Field have

26 recently suffered serious erosion due to extreme storm events and become

27 increasingly vulnerable. In this study, a well validated and tested Delft 3D module by

28 the observing hydrodynamic and sediment data to simulate the hydrodynamics and

29 seabed erosion during a storm event in the littoral area of YRD. Observed wave,

30 current and sediment data under both fair-weather and storm conditions were

31 collected in the study area and used to validate the model. The results indicated that

32 the model can reproduce well the hydrodynamic and sediment transport processes. A

33 series of numerical experiments were carried out to examine the hydrodynamic

34 changes and sediment transports. In the numerical experiment of normal condition,

35 there is hardly any sediment transport off the YRD. The numerical experiment of

36 storm condition showed that storms enhanced tidal residual currents, weakened tidal

37 shear front, and significant wave heights up to 2 m, considerably intensified the

38 sediment resuspension and dispersal. The local sediment resuspension due to the

39 increased wave-induced bottom stress promoted the sediment plume to expand to the

40 central area of Laizhou Bay, which seemed to provide sediment source for offshore

41 and southward transport. During the storm, the active nearshore sediment

42 resuspension provided sediment source for offshore and southward transport. The

43 intensive dynamics and sediment transport under storm conditions caused significant

44 changes in seabed erosion and siltation. The main erosion occurred off the Gudong

45 and northern YRD, while the main siltation appeared in the central area of Laizhou

46 Bay. No significant recovery after a storm and frequent strong winds have an

47 accumulative effect on the erosion, which is very likely to dominate the erosive states

48 of the YRD coast in the future.

49 **Keywords:** Yellow River Delta; Storms; Tidal shear front; Sediment transport;

50 Seabed erosion; Morphodynamics

51 **1   Introduction**

52   Fluvial discharge, wave energy and tidal range are critical in determining

53 morphological evolutions of most deltas worldwide. Sediment input to deltas has been

54 reduced or eliminated (Syvitski and Kettner, 2011; Wang et al., 2011; Dai et al., 2016;

55 Liu et al., 2019), which causes delta erosion and sinking, and increasing delta's

56 wetlands will be drowned (Tessler et al., 2015; Wolters and Kuenzer, 2015; Murray et

57 al., 2019). Lack of knowledge on erosion mechanism and deltaic processes may lead

58 to erroneous conclusions about how deltas function. More recently, sea level rise,

59 insufficient supply of sediment, human interventions and climate changes, which may

60 cause more extreme event, such as flood and storm have been the emerging key

61 factors to reshape mega-deltas (Nicholls and Cazenave, 2010; Blum and Roberts 2009;

62 Yang et al., 2011a; Bi et al., 2014; Liu et al., 2017; Becker., 2020).

63   As we known, hydrodynamic changes and sediment transport control

64 morphological evolution of deltas (Gong et al., 2014; Wu et al., 2015). These control

65 impacts varied at different time scales. Wherein, hydrodynamic changes and sediment

66   transport in storm event can belong to a short-term effect (Ralston et al., 2013;

67   Anthony, 2015; Florin et al., 2017). However, it is difficult to observe them during the

68   storm event. Therefore, the numerical model, which integrate hydrodynamics, wave

69   propagation, sediment transport and morphological changes numerical model, has

70   provided new indispensable tools to examine the effects of storm events. Numerous

71   numerical models have been developed with enhanced capability of simulating the

72   processes of currents, waves, salinities and sediments in delta areas, such as ECOM-si,

73   and FVCOM for estuarine circulations; ECOMSED for sediment transport; SWAN for

74   nearshore wave climates; and many other modelling systems, such as ROMS, MIKE 3

75   (DHI Water and Environment), and Delft3D for regional hydrodynamics and

76   morphodynamics.

77   The YRD has been gradually formed in the western Bohai Sea (Fig. 1a), since

78   the Yellow River migrated its main watercourse from the Yellow Sea to the Bohai Sea

79   in 1855. With the subsequent frequent avulsions both natural and engineered, the

80   YRD has developed several delta lobes (Fig. 1b), and the significant morphological

81   evolution of the abandoned delta lobes have been observed in recent decades. For

82   example, the coastline along the northern YRD and Gudong Oil Field have suffered

83   serious erosion in recent years (Qi and Liu 2017). Moreover, the energetic winds and

84   waves generated by storm events have been found to significantly impact on this

85   coastal region. During storm events, the wave action is particularly prominent off the

86   YRD, becoming a key factor in controlling sediment resuspension (Jia et al., 2012;

87   Zhang et al., 2018). Many studies have addressed its shoreline dynamics (Zhang, 2011;

88   Kuenzer et al., 2014; Fan et al., 2018), morphological changes (Kong et al., 2015; Xu

89   et al., 2016; Jiang et al., 2017; Wu et al., 2017) and sediment dispersals (Wang et al.,

90   2010; Bi et al., 2014; Wu et al., 2015).
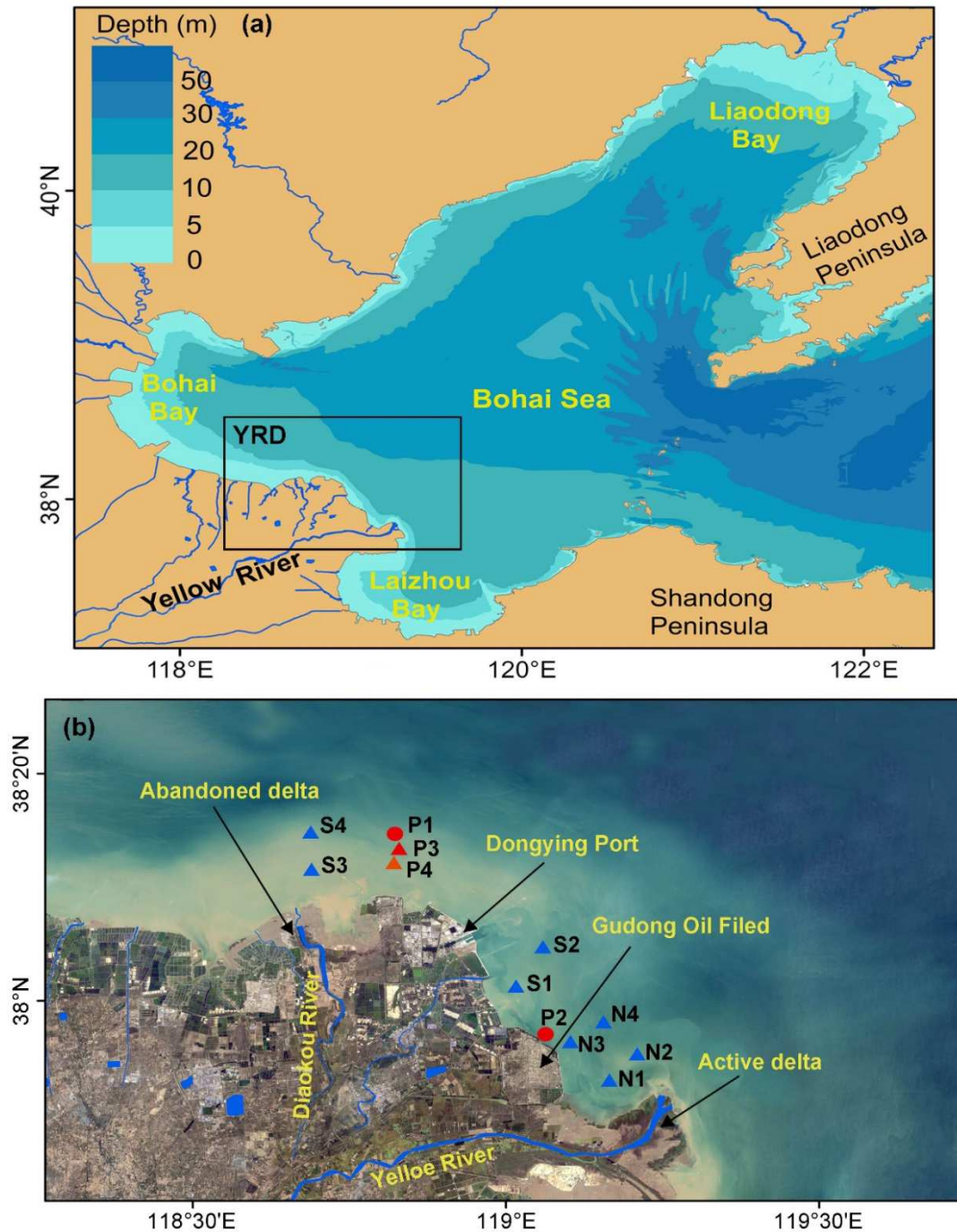
91

92   **Fig. 1.** (a) Computational domain and topography of the Bohai Sea; (b) Detailed study area, where
93   blue triangles mark the locations of the vertical hydrological and sediment measurements and
94   other marks represent the locations of continuous survey during the storm event in April 2013.
95   Two alongshore sections are also indicated for detailed comparisons.

5

96   However, little research has been focused on the storm-induced hydrodynamic

97   and morphological processes, especially in relation to the mechanism of coastal

98   erosion. Therefore, this study focuses on exploring the hydrodynamic and sediment

99   characteristics in the YRD during storms using the Delft3D model together with the

100 measured sediment, wave, and tidal data during a storm event in April 2013, in an

101 attempt to reveal the storm-induced hydrodynamic changes and seabed erosion.

102 ## 2   Model description

103 **2.1 Study area and model grid**

104   The YRD, located in mid-latitude region, is susceptible to storms throughout the

105 year, especially storms generated by cold-air outbreaks in winter, or in

106 autumn-to-winter and winter-to-spring seasonal transition (Wu et al., 2002). Such

107 storms usually lead to intense hydrodynamic changes and significant sea-level

108 anomalies around the YRD nearshore zone. In 2013, 12 storm surges occurred in the

109 littoral area of Yellow River Delta, all of which were extratropical storm (Beihai

110 Branch of State Oceanic Administration People's Republic of China, 2014). Among

111 them, the storm occurring in April 2013 was selected to simulate based on a coupled

112 model, which combines hydrodynamic model (Delft3D-FLOW), wave

113 (Delft3D-WAVE) and sediment transport (Delft3D-SED). In the early stage of this

114 storm, the northwest wind was dominant. On April 13, 2013, the wind direction

115 turned to north, and then gradually turned to northeast. The storm event began at 2:00

116 on April 13 and ended at 3:00 on April 15, and lasted nearly 50 hours from growth to

117 decline, covering two tidal cycles, in which the wind speed maintained at about 20

118   m/s for 20 hours, from 12:00 on the 13th to 8:00 on the 14th (Fig. 2).
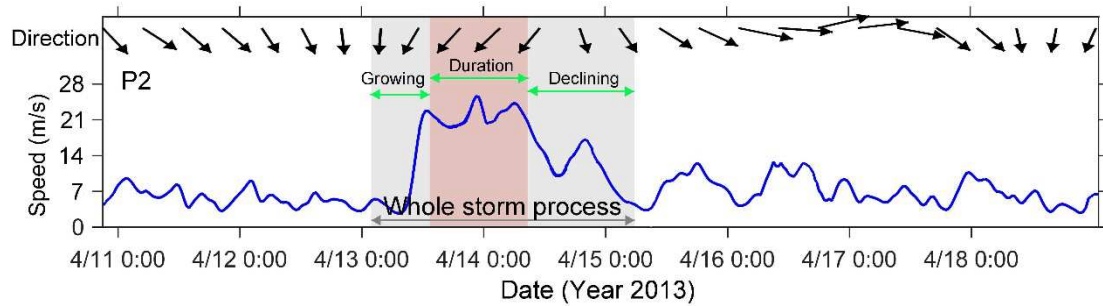

119

120   **Fig. 2.** The wind process during the examined storm.

121   Since the Bohai Sea is a semi-enclosed sea, and cold-air outbreaks mostly occur

122   northerly in this region, the model domain was set to cover the entire Bohai Sea, with

123   an open boundary in the north Yellow Sea near the Bohai Strait. Curvilinear grid cells

124   that cover this domain were generated by Delft3D-RGFGRID with a refined high grid

125   resolution used in the areas of interest at the Yellow River subaqueous delta. The total

126   number of grid cells was 771×432 (Fig. 3 a). The average grid cell spacing was about

127   1 km; varying from the maximum mesh size of nearly 2 km at the open boundaries to

128   the minimum mesh size of approximately 150 m along the YRD coast (Fig. 3 b-d).

129   The topography data were based on the YRD surveys carried out in 2012 for the

130   subaqueous delta, with a spatial resolution of 300-500 m, and coastal surveys carried

131   out in 2009 for the other part of the Bohai Sea, with a spatial resolution of 1000-5000

132   m, respectively (Fig. 3 a). In winter, due to the prevalence of strong northerly wind

133   and concomitant high waves (Bi et al., 2011), the distribution of salinity, temperature

134   and sediment in the littoral area of YRD is found to be vertically homogeneous,

135   indicating a well-mixed water column (Yang et al., 2011). Thus, the model adopted

136   seven layers in the vertical direction, and from the bottom layer to surface layer, the

137   values of σ were set to 0.1, 0.1, 0.2, 0.2, 0.2, 0.1, and 0.1.
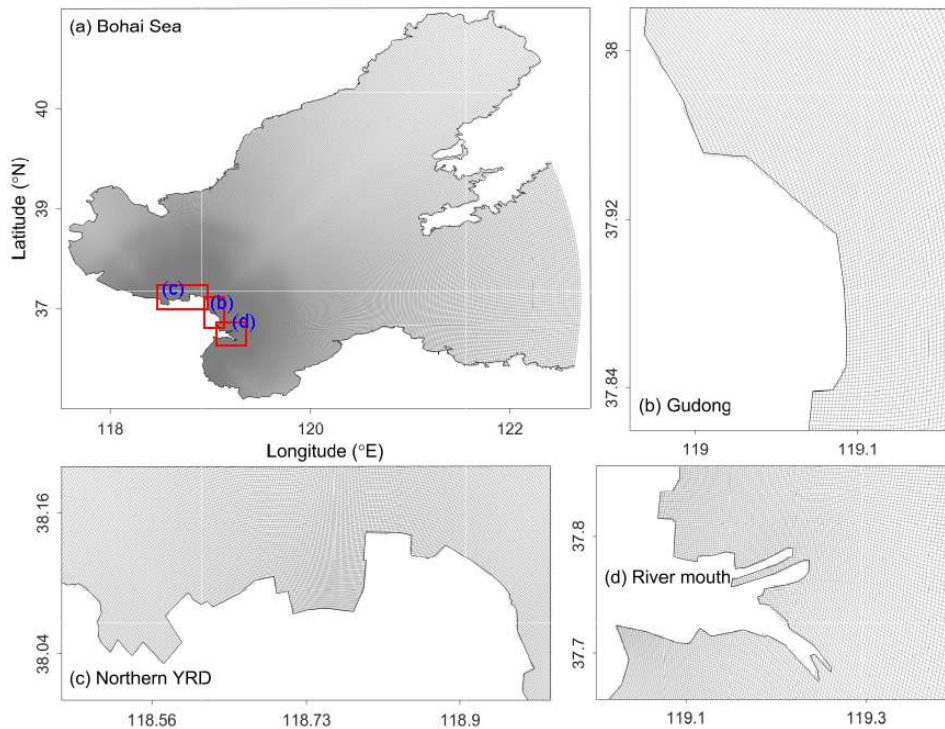
138

139   **Fig. 3.** (a) Numerical model mesh with the details of: (b) the Gudong coast (c) the northern YRD,
140   and (d) the active river mouth. The three red boxes in (a) from top to bottom mark the northern
141   YRD, the Gudong coast and the active river mouth, respectively.

142   **2.2 Initial and boundary conditions**

143   Using the modelling system above described, simulations started initially with a

144   static state from the mean sea level, and zero flow velocity and sediment

145   concentration in the domain. The coastline boundaries were determined from the

146   high-water lines with a spatial resolution of 15 m, which were extracted from the false

147   color composite images of Landsat OLI data. The model was driven by the tide

148   forcing along the open boundary, consisting of 8 main tidal constituents, i.e. M2, S2,

149   N2, K2, K1, O1, P1 and Q1, as well as surface forcing from the ECMWF (European

150   Centre for Medium-Range Weather Forecasts) wind and atmospheric pressure data

151   with a spatial resolution of 0.25°×0.25° (latitude× longitude). Compared with the

152 storm scale in the Bohai Sea, this resolution is sufficient for modeling land-ocean

153 gradients (Lv et al, 2014).

154   Suspended sediment concentration (SSC) at seaward boundary was set to 0, since

155 the open boundary is far from the interested area and the water depth is mostly deeper

156 than 30 m, so that the impact of sediment conditions from the open boundary on the

157 sediment transport in the nearshore region which was based on the local equilibrium

158 transport formula can be neglected. At landward boundary, distinct seasonal variation

159 of sediment delivery occurs from the Yellow River. River discharge boundary

160 conditions were imposed appropriately based on daily-averaged water discharge and

161 sediment concentration recorded from the Lijin hydrological station, provided by the

162 Yellow River Water Resource Commission.

163 **2.3 Parameter settings**

164   The bottom friction was parameterized using the Manning coefficient n,

165 calculated from the water depth (Xing et al., 2012):

$$n=(0.015 + 0.01/h) \quad , \quad h>1 \qquad (1)$$

166 where h is the water depth (m). The bottom roughness for regions water depth below

167 1 m is prescribed by a uniform Manning coefficient of 0.025, which is the result of

168 verification of the coupled model. It should be noted that the Manning coefficient was

169 defined differently in Delft3D as $M_n=1/n$. The horizontal eddy viscosity and

170 diffusivity are calculated with the Horizontal Large Eddy Simulation (HLES) sub-grid

171 model.

172   According to Ren et al. (2012), the seabed composition off the YRD is highly

173   variable in space, and the median grain size (D_{50}) varies widely from ~ 5 to ~133 μm.

174   Therefore, multiple sediment fractions were considered in the morphological model.

175   In this study, four mud fractions (fine to coarse, denoted as md1–md4) were used to

176   represent nearly the full range of cohesive sediment grain sizes (4, 7.5, 28, and 62.5

177   μm). Specifically, one sand fraction (100 μm) was included in the model, i.e., the

178   dominant fine sand fraction (denoted as sd1), to reduce the overestimation of erosion

179   along the coasts. The settling velocity (w_s) of each mud fraction was determined

180   relative to the grain size after calibrating the model against the spatial distribution of

181   depth-averaged SSC.

182   Critical erosion shear stress τ_{ce} was a key parameter for simulating fine-grained

183   sediment transport. For the critical shear stress of the cohesive sediment, the

184   following formulas were used (Dou, 1999; Lu et al., 2011):

$$\tau_{ce}=k^2\rho\,(\frac{d^{'}}{d^*})^{\frac{1}{3}}\left[3.6\frac{\rho_s\text{-}\rho}{\rho}gD_{50}+(\frac{\gamma_0}{\gamma_0*})^{\frac{5}{2}}(\frac{\varepsilon_0+gh\delta\sqrt{\delta/D_{50}}}{D_{50}})\right] \qquad (2)$$

185   where ρ_s is the specific sediment density, 2650 kg m^{-3}; ρ is the fresh water density,

186   1000 kg m^{-1}; g is gravity acceleration, and D_{50} is median size of sediment; ε_0 is

187   comprehensive cohesion coefficient, 1.75 cm^3/s^2; k is a coefficient of different status

188   of incipient motion, 0.128; δ is the thickness of pellicular water, and $\delta = 2.31\times10^{-5}$

189   cm. In this study, $d^{'} = 0.5$ mm when $D_{50} < 0.5$ mm, and $d^* = 10$ mm accordingly.

190   Initial dry bulk density γ_0 is:

$$\gamma_0=\rho_s(1\text{-}e_0\eta) \qquad (3)$$

191   and steady dry bulk density γ_0* is:

$$\gamma_0{}^* = \rho_s \left(1 - \frac{\pi}{6}(1 - 2\sqrt[3]{D_{50}})\right) \qquad (4)$$

192 where e_0 is the maximum porosity, and we used $e_0 = 0.625$. For all the mud

193 fractions, the erosion parameter M is 5.0×10^{-5} kg/m^2/s, the specific density is 2650

194 kg/m^3, and the dry bed density is 500 kg/m^3.

195   The erosion and deposition fluxes for cohesive sediment ($<$ 64 μm) were

196 calculated applying the following Partheniades-Krone formulations:

$$E_i = M_i \left(\frac{\tau_b}{\tau_{b,i}} - 1\right), \text{ when } \tau_{cw} > \tau_{cw,i}, \text{ else } E_i = 0 \qquad (5)$$

$$D_i = w_{s,i} c_{b,i} \qquad (6)$$

197 where E_i, D_i and M_i are the erosion flux, deposition flux and erosion parameter of

198 the ith mud fraction (kg/m^2/s), respectively; $w_{s,i}$ is the settling velocity of the ith mud

199 fraction (m/s); $c_{b,i}$ is the depth-averaged concentration of the ith mud fraction

200 (kg/m^3); τ_b is the combined bed shear stress due to currents and waves (N/m); and

201 $\tau_{b,i}$ is the critical shear stress for erosion of the ith mud fraction (N/m^2). For 2D

202 depth-averaged flow bed shear stress induced by a turbulent flow is assumed to be

203 given by a quadratic friction law:

$$\tau_b = \frac{\rho_0 g \vec{U} |\vec{U}|}{C_{2D}^2} \qquad (7)$$

205 Where $\vec{U}$ is the magnitude of the depth-averaged horizontal velocity. Due to finest

206 fractions can be entrained into the seabed (Winterwerp et al., 2007), the critical shear

207 stress for deposition was omitted in the model, which means that continuous

208 deposition was specified in the model. All those parameters used in the mode

209 simulations are summarized in Table 1.

11

210   **Table 1**

211   Sediment and mud fractions considered in the morphological model

Type	Fraction	D_{50} (μm)	τ_{ce} (N/m^2)	w_s (mm/s)	M (kg/m^2/s)
Mud	md1	4	Spatially varying	0.06	5.0×10^{-5}
	md2	7.5		0.14	
	md3	28		0.22	
	md4	62.5		0.26	
Sand	sd1	100	−	−	−

212   The sediment transport processes responsible for bed-level changes vary greatly

213   off the YRD due to the spatial variations of the bed sediment grain size. Therefore,

214   our model considers both non-cohesive (sand) and cohesive sediment (mud), which

215   are treated separately in Delft3D, and sand-mud interactions are excluded as a first

216   approximation. Suspended sediment transport is calculated by solving the

217   depth-averaged advection-diffusion equation, which includes source and sink terms

218   and is presented below:

$$\frac{\partial h c_i}{\partial t} + \frac{\partial h u c_i}{\partial x} + \frac{\partial h v c_i}{\partial y} = \frac{\partial}{\partial x}(h \varepsilon_h \frac{\partial c_i}{\partial x}) + \frac{\partial}{\partial y}(h \varepsilon_h \frac{\partial c_i}{\partial y}) + S_i \qquad (7)$$

219   where c_i is the sediment concentration of the ith sediment fraction (kg/m^3), u and v

220   are horizontal velocity components (m/s), ε_h is horizontal eddy diffusivity (m^2/s),

221   and S_i is the source and sink term of the ith sediment fraction representing the

222   exchange between the water colum and the bed. For non-cohesive sediment transport

223   (≥ 64 μm), we follow the approach of Van Rijn (1993).

224   3   Model validations

225   3.1 Tidal regime

226   The tides in the Bohai Sea are relatively small and fall into the

227   micro-tidal/mixed-semidiurnal categories. Tides from the northwest Pacific

228 propagates into the Bohai Sea through the Bohai Strait. There are two amphidromic

229 points for semidiurnal tidal constituents (M2 and S2) in the Bohai Sea: one at the

230 offshore area of Qinhuangdao and the other near the Yellow River mouth. One

231 amphidromic point for diurnal tidal constituents (K1 and O1) appears in the Bohai

232 Strait. The tidal model ran 30 days in order to obtain tidal constituents harmonic

233 constants. Harmonic constants of tidal elevation of each constituent are obtained by

234 applying harmonic analysis to modeled time series of sea level at each model grid.

235 The results showed that our model successfully simulated tide systems. The co-tidal

236 and co-range lines for M2, S2, K1, O1 constituents (Fig. 4) fitted well with

237 observations (Chen et al., 1992) and the results of Huang (1995). The changes of the

238 YRD influenced its surrounding tidal wave and obstructed tidal energy (Pelling et al.,

239 2013), and the amphidromic points here calculated using new coastlines were farther

240 to land than previous studies. Also, this result agreed well with other publications

241 (Hao et al., 2010).
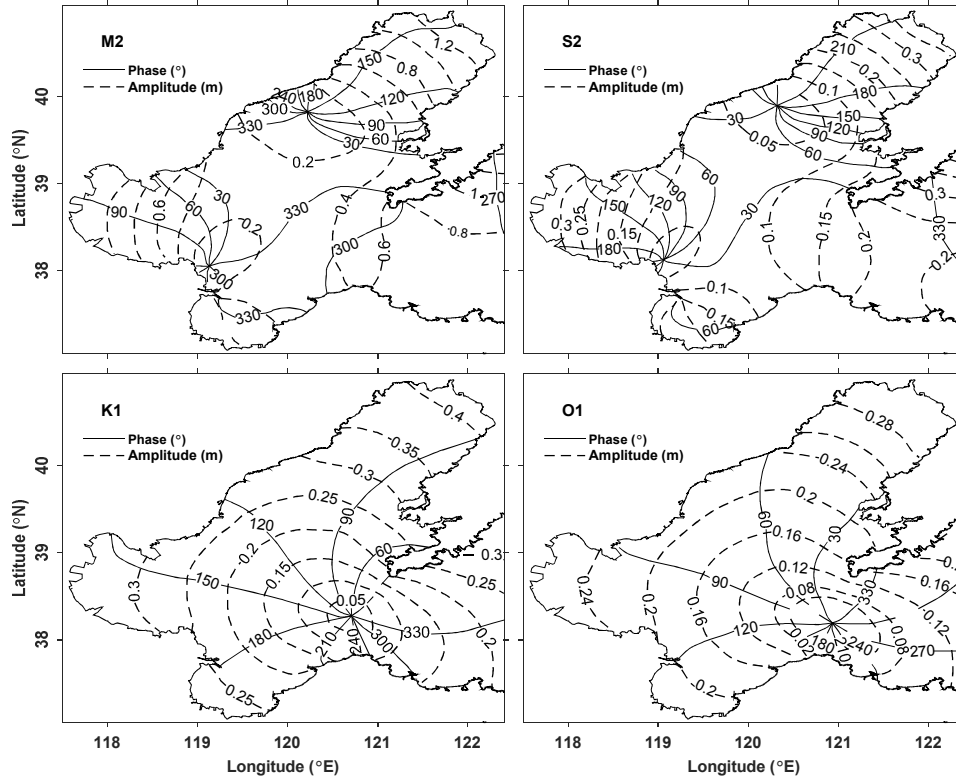
242
243 **Fig. 4.** Co-tidal charts of M2, S2, K1, O1 constituents from the model simulations (dotted and
244 solid lines indicating the amplitude and phase, respectively.

245 **3.2 Tide velocity**

246 The accurate prediction of flow velocity and direction was a crucial step for the

247 simulations of sediment transport which strongly depends on the shear stress,

248 deposition criterion, and turbulence characteristics in the bottom boundary layer. The

249 time series of currents and SSCs measured along the YRD coast were used to validate

250 the model in normal conditions. The observations were taken at eight sites, as shown

251 in Fig. 1b, at N1, N2, N3 and N4 in July 2009, and S1, S2, S3 and S4 in October 2009.

252 The correlation coefficient (CC), the skill score (SS), and the root mean square errors

253 (RMSE) were calculated to evaluate the quality of the model performance:

$$CC = \frac{\sum (X_{mod} - \overline{X_{mod}})(X_{obs} - \overline{X_{obs}})}{[\sum (X_{mod} - \overline{X_{mod}})^2 \sum (X_{obs} - \overline{X_{obs}})^2]^{1/2}} \qquad (8)$$

$$SS = 1 - \frac{\sum (X_{mod} - X_{obs})^2}{\sum (X_{mod} - \overline{X_{obs}})^2} \qquad (9)$$

14

$$RMSE=\sqrt{\frac{\sum(X_{mod}-X_{obs})^2}{N}} \qquad\qquad (10)$$

254   where X_{mod} is the modeled result and X_{obs} is the observed data. The performance of

255   model is classified as suggested by Allen et al., 2007; Ralston et al., 2010; Luo et al.,

256   2017 as show in Table 2.

257   **Table 2**

258   Classification of model performance

SS	>0.65	0.65-0.5	0.5-0.2	<0.2
Performance	Excellent	Very good	Good	Poor

259   We first validated the simulations with the normal conditions. The model

260   simulation began June 15, 2009. After running for half a year with the observed runoff

261   and 6-hourly ECMWF re-analyzed wind, the model results were output for

262   comparison. Comparisons of the depth-averaged flow velocity and direction with the

263   model results and the observation data are shown in Fig. 5. The type of tidal current

264   was semidiurnal and rectilinear, and the velocity curve showed four peaks and four

265   valleys within one day. Statistical assessments of validation are shown in Table 3. It is

266   clear that the average *CC* of flow velocity at N1-N4 was 0.78, which was lower than

267   those at S1-S4, 0.89, because those sites locate at the river mouth, the estuarine

268   circulation is rather complicated. The average *SS* at S1-S4 and N1-N4 was 0.62 and

269   0.49 (Table 3), respectively, ranking ''very good'' and ''good'' according to the

270   categories described above. The *RMSE* were also reasonable.

271
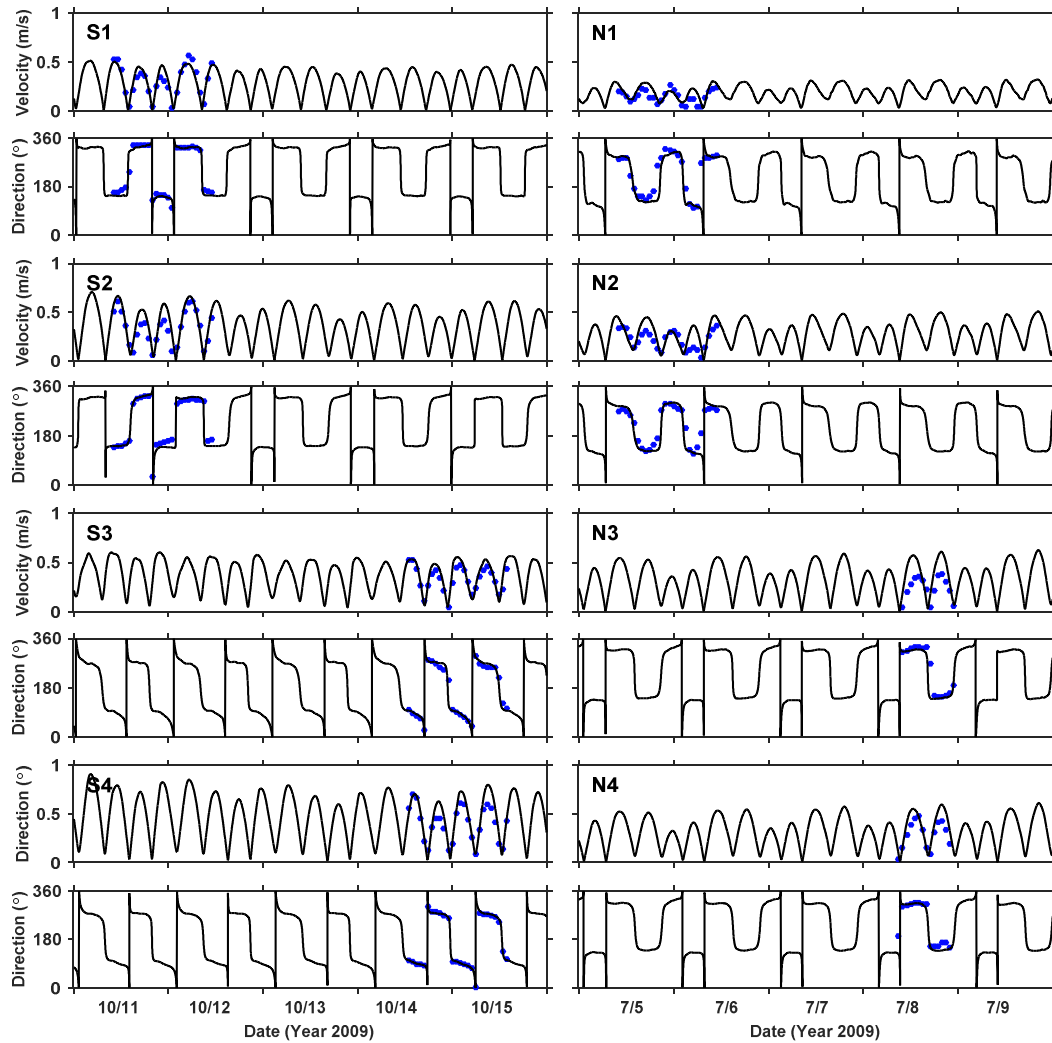
Fig. 5. Comparison of measured depth-average flow velocity and flow direction (blue dots) with the computed results (solid line) at eight measurement locations.

3.3 Suspended sediment concentration

The computed SSCs were compared with the observed SSCs at Sites S1-S4 and N1-N4 (Fig. 6). The computed SSC was well reproduced with tidal variation. For example, the tide had a transition from spring tides to neap tide during Oct 11 to Oct 15, 2009, so the modeled SSCs of sites S1-S4 during the period had decrease trends. The modeled SSC had the same order of magnitude as the measurements. The relatively large errors between the modeled and observed data appearing at sites S3 and S4 were mainly due to the erosion caused by waves, which was difficult to

282   estimate during neap tides. The average *SS* of SSC at sites S1-S4 and N1-N2 (not with

283   N3 and N4 because of less samples) were 0.24 and 0.26 (Table 3), indicating that the

284   model preformed satisfactory. The *CC* and *RMSE* in Table 2 also illustrated the good

285   performance of the model. The results clearly indicate that the model was properly set

286   up and can be used to study the dynamics of sediment process off the YRD coast

287   during normal conditions.
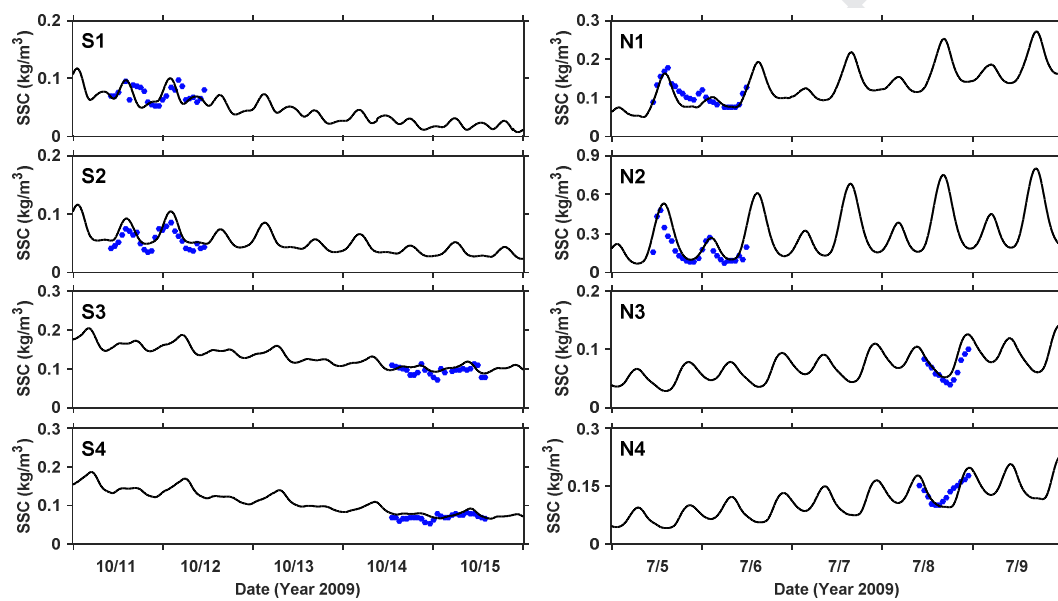
288

289   **Fig. 6.** Comparison of depth-average flow velocity and flow direction between the simulated
290   (solid line) and the observed (blue dots) at eight sites.

291   **Table 3**
292   Correlation Coefficient, Root-Mean-Square Error, and Skill Score of each measured site

	S1-S4 (average)			N1-N4 (average)		
	CC	SS	RMSE	CC	SS	RMSE
Velocity (m/s)	0.89	0. 62	0.08	0.78	0.49	0.11
SSC (kg/m^3)	0.57	0.24	0.05	0.62	0.26	0.04

293   **3.4 Storm validations**

294   The measured data during a storm in April 2013 were employed for storm

295   verification of hydrodynamic and sediment characteristics. More details of this survey

296   can be seen in the work by Quan (2014) and Bian et al (2016). The water levels data

17

297 were provided by Central Platform of Shengli Oil Field (P1, locations are labeled in

298 Fig. 1b) and Gudong gauge station (P2). The flow and wave data were collected with

299 an ADCP (Acoustic Doppler Current Profilers) at P3, and the SSC data were collected

300 with a turbidity meter (OBS-3D) at P4.

301 To verify the accuracy of the coupled Delft3D-WAVE model, the P3 site was

302 selected to compare the wave height and period between observation and simulation

303 during the storm period of April 15-17 2013 (Fig. 7). The SWAN model generally

304 well-reproduced variations of the significant wave height and period (Fig. 7a). A cold

305 front passed on the April 13, resulting in a marked increase in wave height (maximum

306 wave height of approximately 2.0 m). The simulated wave heights were slightly

307 underestimated due to the low temporal resolution of the meteorological forcing,

308 which was unable to capture the peaks of wind velocities values adequately. The skill

309 assessments are summarized in Table 4. The *SS* of wave height was 0.41, ranking

310 "good" according to the categories described above. The *CC* and *RMSE* were also

311 reasonable. Through comparison between simulated and observed storm tide at P1

312 and P2 sites (Fig. 7b), the maximum and minimum water level as well as the phase

313 were in reasonable agreement with the measurements. The *SS* of storm tide at site P1

314 and P2 was 0.26 and 0.27, respectively, which indicated the reasonableness of storm

315 tide verification. The flow and SSC validations are shown in Fig. 7c and Fig. 7d. The

316 model reproduced a similar sectional pattern to the survey, specifically, the *SS* of flow

317 velocity and SSC were 0.51 and 0.21, and the *CC* were 0.65 and 0.49, respectively.

318 Verification results showed that model predictions during storm period based on the

319   model were quite consistent with the observations at these sites.
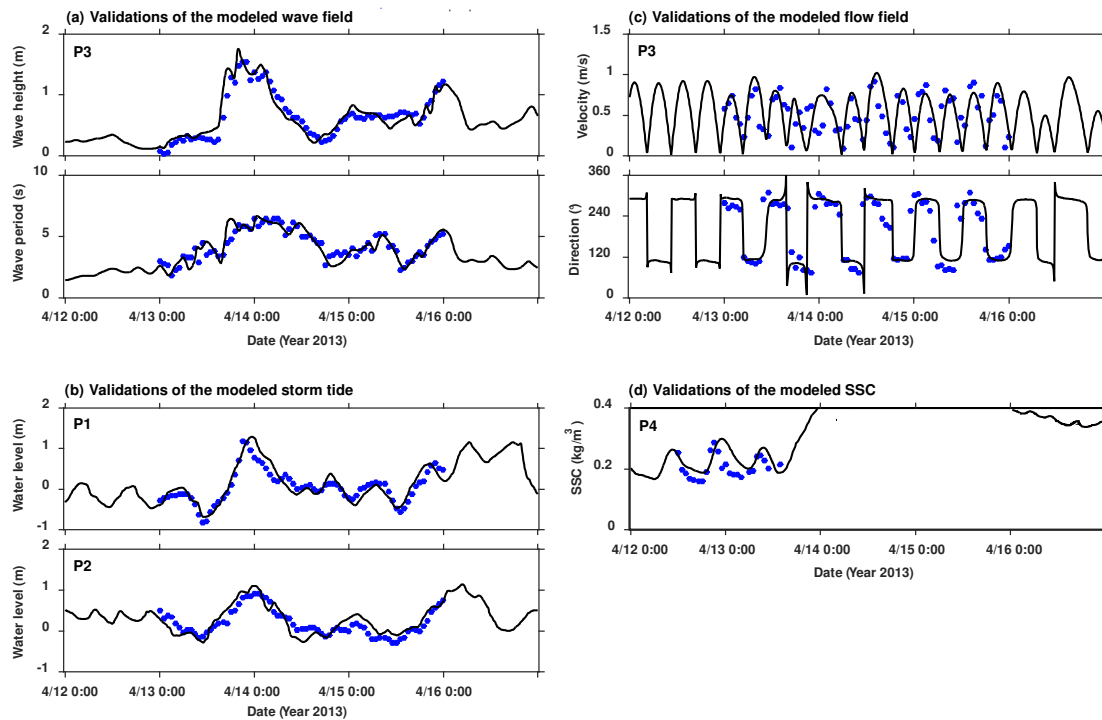
320

321   **Fig. 7.** Comparison of depth-average flow velocity and direction between the simulated (solid line)
322   and the observed (blue dots) at eight sites.

323   **Table 4**

324   Correlation Coefficient, Root-Mean-Square Error, and Skill Score of each measured site

	P1, P2 (average)			P3			P4		
	CC	SS	RMSE	CC	SS	RMSE	CC	SS	RMSE
Wave height (m)	-	-	-	0.84	0.71	0.13	-	-	-
Storm surge (m)	0.89	0.73	0.18	-	-	-	-	-	-
Velocity (m/s)	-	-	-	0.65	0.51	0.11	-	-	-
SSC (kg/m^3)	-	-	-	-	-	-	0.49	0.21	0.06

325   # 4   Results and discussion

326   In total, three runs were considered in this study to examine the impacts of storm

327   conditions on hydrodynamics and sediment transport over the nearshore seabed of

328   YRD, as shown in Table 5. Run 1 (control run) was embedded into a

329   wave-tide-circulation coupled model and driven by climatological daily mean river

330   discharge and calm wind (speed below 3 m/s) as well as water flux and salinity in

331   open ocean boundary. We can understand the characteristics of hydrodynamics and

19

332 sediment in normal conditions from the control run. In Run 2, the calm wind and

333 normal atmospheric pressure conditions used in Run 1 were replaced by strong wind

334 and low atmospheric pressure conditions (data from ECMWF) for setting storm

335 conditions. By comparing the results of these two runs, we can quantitatively identify

336 storm impacts. In addition, Run 3 was conducted with storm conditions without tides.

337 The impacts of storm-induced wave on the seabed erosion were examined by

338 comparing the results of three runs.. All the numerical experiments were run over a

339 period of one month, beginning on April 1, 2013, and the data calculated by the model

340 from April 13 to April 15 were used to analyze the hydrodynamic processes and

341 sediment transport.

342 **Table 5**

343 Three different conditions for model simulations

Simulation	Tide	Wind	Waves
Run 1 (control run)	Yes	No (normal condition)	Yes
Run 2	Yes	Strong	Yes
Run 3	No	Strong	Yes

344 **4.1 Waves**

345 Calm winds forcing for Run 1 typically produced waves with significant wave

346 height of less than 0.8 m (Figure 8a), and period of less than 3 s in the study area. The

347 weak wave dynamic is attributed to the causes of wave in this area. The Bohai Sea has

348 poor water exchange capacity with open ocean due to its narrow strait occupied by

349 islands. Surface waves are generated by local winds.

350 The time series of wind stress for Run 2 are shown in Fig. 8c from April 12 to 14,

351 2013. The wind vectors were surface area averaged off the YRD, and on the

352 conventional geographical coordinate system. As shown in the Fig. 8c, strong wind

20

353 (more than 12 m/s) began in the morning of April 13 with directions moved from

354 northwest to the northeast on April 13 and moved the northwest again on April 14.

355 The northeasterly wind speeds shown two acceleration processes, in the morning and

356 the end of April 13, respectively. The results from Run 2 showed that the wave height

357 of approximately 2 m along the Gudong coast under the maximum wind speed, and

358 the wave height of more than 1.2 m along the northern YRD coast (Fig. 8b). The time

359 series of significant wave height, direction and period of site N3 is presented in Fig.

360 8d to show the changes at temporal scales of wave features. It can be seen that the

361 significant wave height and period were generally accordant with wind speed, and the

362 wave directions changed with wind directions. The significant wave height reached its

363 maximum, more than 2 m, at site N3, during the first wind acceleration process of

364 northeasterly wind, and reached more than 1.5 mduring the second wind acceleration

365 process.
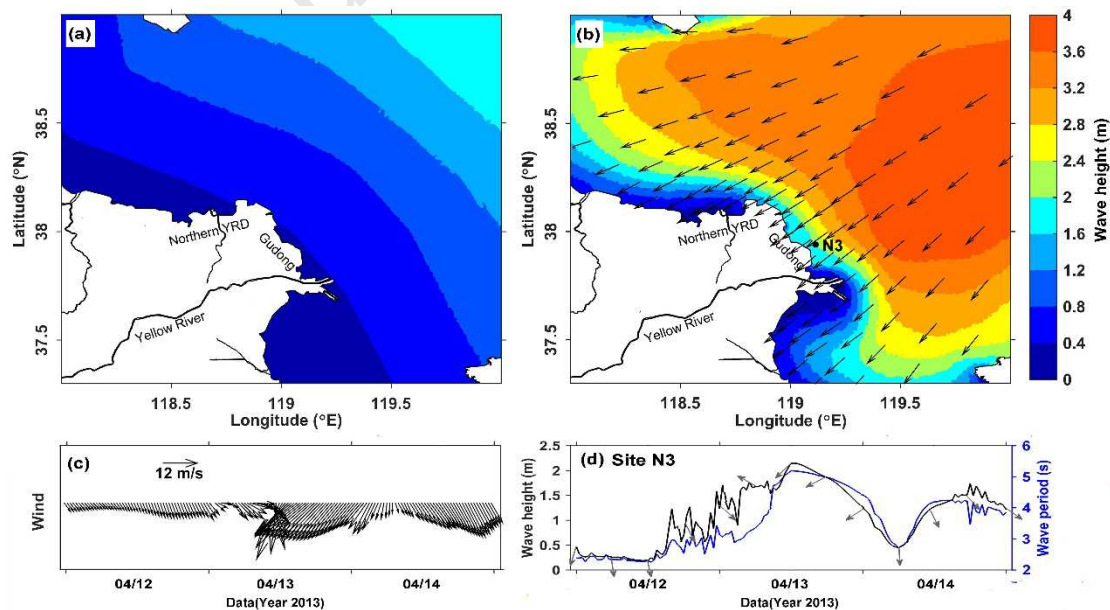
366

367 **Fig. 8.** (a) Significant wave height during calm condition forcing for Run 1. (b-d) Wave features
368 during the examined storm: (b) significant wave height and direction with the maximum wind
369 speed; (c) time series of surface area averaged wind vector off the YRD (118-120°E, 37.3-38°N);

370   (d) significant wave height (black line), direction (gray arrow) and period (blue line) at site N3.

371   **4.2 Currents**

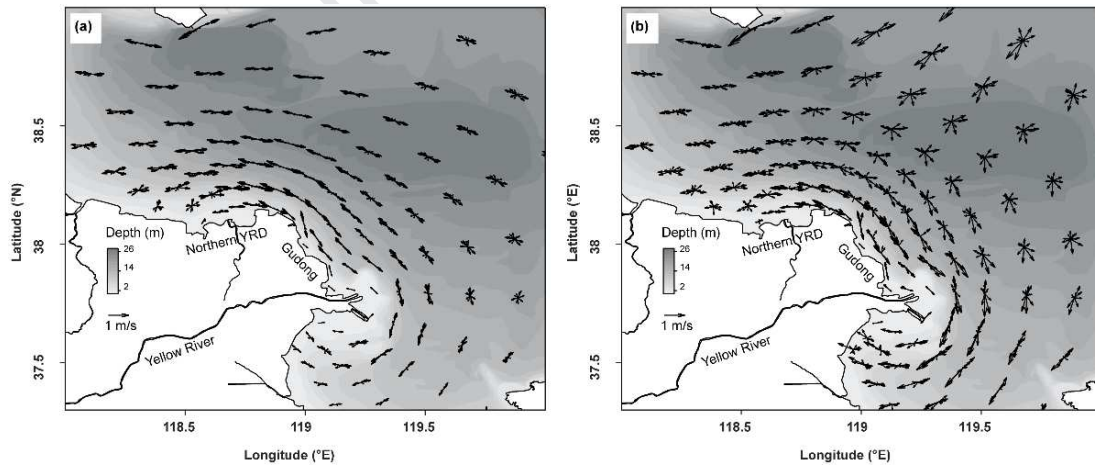372   *4.2.1 Water mass transport*

373   Storm-induced seaward coastal sediment transport can be key for to the inner

374   shelf (Goff et al., 2010). To investigate the impacts of storm-surge flood and ebb on

375   sediment transport, we first examined storm-induced current fields. The model runs

376   were either forced by calm wind (Run 1), or strong northerly wind (Run 2). Fig. 9a

377   shows the current was reciprocated with southeastern flood and northwestern ebb in

378   normal conditions, with areas of high current velocity locating off the northern YRD

379   coast and the active river mouth. Reciprocated current was predominant in shallow

380   area (roughly within the 15m isobaths), while it gradually turned into rotated current

381   with the increase of water depth. In storm conditions, not only the current velocities

382   increased, especially the flood velocity, but the directions were also changed: rotated

383   current was predominant (Fig. 9b). Special attention should be paid to the feathers in

384   the shallow area: most of these current vectors were along the flood-ebb axis or

385   directed to the right side of the ebb direction. Nonlinear interaction between the tide,

386   wind-driven current, and the Coriolis force should be responsible for this phenomenon.

387   Huang et al. (1996) and Cao and Lou (2011) suggested that on the surface, the

388   wind-driven current flows along the wind direction. During flood tide, wind-driven

389   current added to tide current, the water mass could flow to southeast with higher

390   velocity. During ebb, when the sea surface elevation decreases, the tidal water

391   returned to the outlets hard and flowed north-northwestward, opposing with

392   wind-driven current, and the water mass could turn into right-neighbored outlets.

393 Wind intensity and direction can generate changes in residual currents in the shallow

394 areas, which are also found in the shore of the Tagus Estuary (Vaz and Dias, 2014).

395 In order to quantitatively reveal the contributions of the storm to water mass

396 transport, the residual transport of water (Tr_w) through a unit width was calculated,

397 which can be defined as follows:

$$Tr_w = \frac{1}{T} \int_0^T \int_{-H}^{\eta} \vec{V}(x,y,z,t) \mathrm{d}t \qquad (11)$$

398 where η is the surface elevation, H is the still water depth, and $\vec{V}$ is the horizontal

399 velocity vector, and T is the time period. Previous studies (Wu et al., 2014, 2018)

400 showed that residual transport velocity is a more reasonable method than the Eulerian

401 residual current to index the subtidal transport in the shallow coastal water. In this

402 study, 3 d (from 0:00 on April 13 to 16 April), were used as an statistical time window

403 to obtain the Tr_w in normal and storm conditions, respectively, as shown in Fig. 10.

404

405 **Fig. 9.** Tide velocity vectors of depth-averaged current during an ebb-flood process in (a) normal
406 conditions and (b) storm conditions.
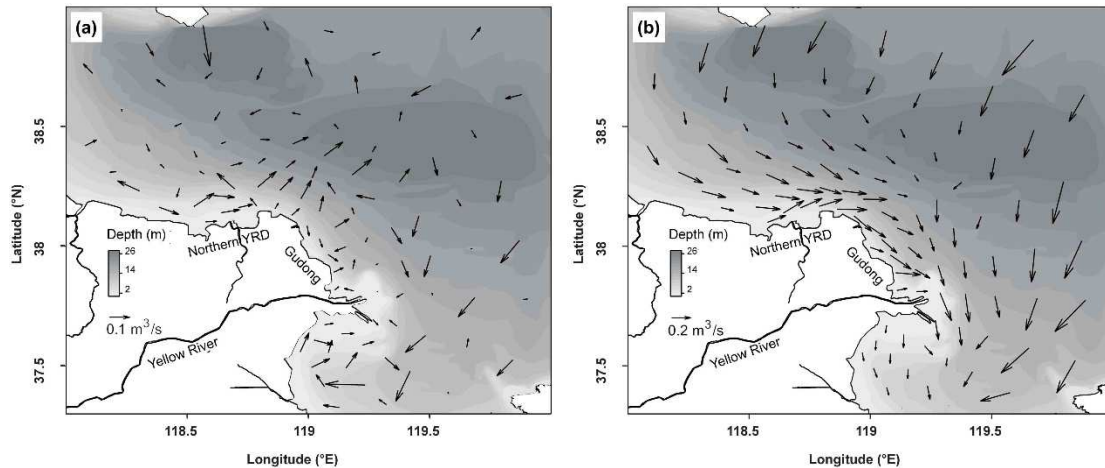
Fig. 10. Residual water mass transport in (a) normal and (b) storm conditions.

In normal conditions, the influence of wind was weak, and the residual currents were greatly affected by tidal current. In the shallow area, the Tr_w was generally less than 0.1 m³/s. Affected by the northerly strong wind, the residual transport of water was transported southward in storm conditions, and the Tr_w was generally greater than 0.2 m³/s, which was 2 to 4 times as large as that in normal conditions. Deep water mass transports southwest as a whole, while it begins to transports southeast gradually after reaching the central part of the Bohai Bay. Off the northern YRD, the residual currents flow eastward along the E-W coast. The direction of residual current along the Gudong coast was southeast in storm conditions, basically consistent with it in normal conditions. While, converging the water masses from the shallow area of the Bohai Bay and the northern YRD, and supported by the water mass from deep area, water mass in this area performs a notable transport rate, which was 4 times larger than it in normal conditions. The water transport rate off the river mouth also significantly increase, and massive water was transported to the central area of the Laizhou Bay with the northward inflow. This water transport model also explains why high water level always occurs in the Laizhou Bay and the Bohai Bay during storms

24

425 (Li et al., 2016).

426 *4.2.2 Tidal shear front*

427   Tidal shear front is an interface between two water bodies with opposing flow

428 directions and significant low velocity zone, which are instantaneous extraordinary

429 gradients closely related to sediment dynamics and morphological variabilities (Wang

430 et al., 2007). Tidal shear front in the littoral area of the YRD has been observed and

431 modeled in the previous studies (Qiao et al., 2008; Wang et al., 2017). The front was

432 first reported by Li et al. (1994) who concluded that the shear front, occurring twice

433 during a tidal cycle, could be classified into two types: inner-flood-outer-ebb (IFOE)

434 and inner-ebb-outer-flood (IEOF).

435   From Run 1, both types of tidal shear front were observed in normal conditions,

436 and shown in Fig. 11a and Fig. 11c, respectively. The IEOF type was closer to land

437 and grows to the northern YRD with larger range than the IFOE type. While, strong

438 winds had a predominant impact on tidal shear front. Under the pressure of northerly

439 wind, both the IFOE type (Fig. 11b) and the IEOF type (Fig. 11d) have been

440 weakened with smaller ranges of tidal shear front than in the normal conditions.

441 Besides, the trends of tidal shear front changed to be perpendicular to the coasts

442 comparing with the parallel trends in normal conditions, and the low velocity zones

443 along the YRD coast disappeared, especially at the IFOE type happens (Fig. 11b).

444 These changes of tidal shear front were because of the formation of rotated currents in

445 deep area in strong wind circumstance: tides through rotated currents complete phase

446 changes, not entirely form oppose-direction flow in shallow area. The changes such as

25

447 weakened shear front, disappearance of low velocity zone, were benefit for the

448 sediment resuspension and dispersal.
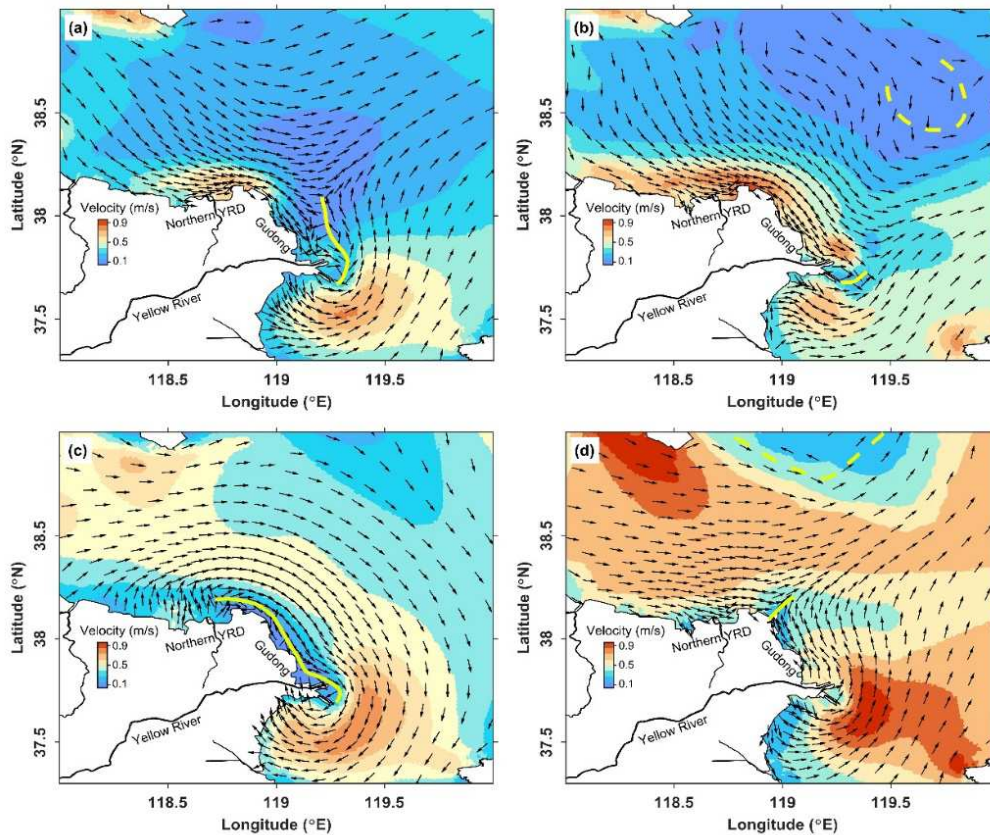
449

450 **Fig. 11.** Locations of tidal shear front of (a) and (b) IFOE type in Runs 1 and 2; and (c) and (d)
451 IEOF type in Runs 1 and 2. The yellow solid lines represent the fronts, and the dashed lines
452 represent the ranges of rotated currents.

453 **4.3 Sediment process**

454 *4.3.1 SSC*

455   The suspended sediment off the YRD is either introduced by river sources or

456 resuspended from the seabed in response to various forcing conditions. We first

457 performed process study to examine suspended sediment distributions. The simulated

458 distribution of depth-averaged SSC from Run 1 and Run 2 are shown in Fig. 12a and

459 Fig. 12b, respectively. When using Landsat data to create sediment color images, we

460 can estimate the simulated results. For example, we chose the Landsat ETM+ data for

26

461   22 March 2014 (3.6 m/s average wind speed at S1-S4 and N1-N4) and 27 November

462   2012 (10.2 m/s average wind speed at S1-S4 and N1-N4) to show the turbid water

463   distribution in normal and storm conditions, respectively. The model reproduced

464   distribution of SSC matches well with the satellite images in Fig. 13, and compared

465   well with the observed data (Yang et al., 2011b; Wang et al., 2014) and the satellite

466   ocean color data (Zhang et al., 2014).

467   Bottom shear stress is an important dynamic factor for sediment erosion and

468   deposition. When the bottom shear stress is greater than the critical bottom shear

469   stress, the bottom sediment will be suspended. The total bottom shear stress (τ_{cw}) is

470   composed of current-induced bottom shear stresses (τ_c) and wave-induced bottom

471   shear stresses (τ_w) under wave-current interaction. The τ_c and τ_{cw} could be obtained

472   from the Run 1 and Run 2, by Formula (7). To further understand the effect of τ_w on

473   the formation of the sediment plume, a numerical Run 3 was conducted in which only

474   wave and strong wind were included. Fig. 14a, 14b and Fig. 14c show the 3-day

475   average τ_c, τ_w and τ_{cw} in the storm conditions, respectively.

476   High SSC values were observed in two regions under normal conditions (Fig.

477   12a) and formed two substantial sediment plumes, one nearshore the northern YRD

478   and the other at the active river mouth, with a value about 1.5 kg/m^3. The sediment

479   plume of the river mouth diffuses to the south, which results in the higher SSC in the

480   northern area of Laizhou Bay. Off the Gudong coast, the SSC was relatively low, less

481   than 0.5 kg/m^3. The distribution of high and low SSC is consistent with that of τ_c

482   (Fig. 14a), which indicates that the τ_c is strong enough to stir the bottom sediment,

483 and formed the sediment plumes off the northern YRD and the river mouth.

484   Compared with the normal conditions, the ranges of high SSC area enlarge

485 significantly under storm conditions (Fig. 12b). The maximum SSC off the northern

486 YRD and the active river mouth was more than 2.6 kg/m^3. High SSC was profound

487 off the Gudong coast, which was 3 times as large as that in normal conditions, with a

488 maximum value of 2.5 kg/m^3, appearing at the most prominent point of Gudong dyke

489 toward the sea. Off the river mouth, the weakened shear front and disappearance of

490 low velocity zone were benefit for the sediment dispersal. Thus, the sediment plume

491 of the river mouth diffuses to the central area of the Laizhou Bay, which causes high

492 SSC appearing at this area.

493   The characteristics of SSC distribution were related to the τ_w and τ_{cw} under

494 storm conditions. The τ_w was higher along the Gudong coast due to larger wave

495 height, where its value reached approximately 1.0 N/m^2 (Fig. 14b). The high value of

496 τ_w at the river mouth was attributed to the shallow water of the mouth bar. In the most

497 of the littoral area of YRD, the τ_{cw} reached approximately 1.1 N/m^2 (Fig. 14c), and

498 the Gudong coast with larger values which was attributed to the higher τ_w (Fig. 14b).

499 This fact indicates that the high SSC along the Gudong coast is generated by local

500 sediment resuspension in storm conditions. During storms, researchers found that the

501 waves as an important agent in the reworking and retreat at the mud-rich deltas that

502 are generally considered as either 'river-dominated', such as the Mississippi (Anthony,

503 2015) or 'tide-dominated', such as the Chao Phraya (Uehara et al., 2010).
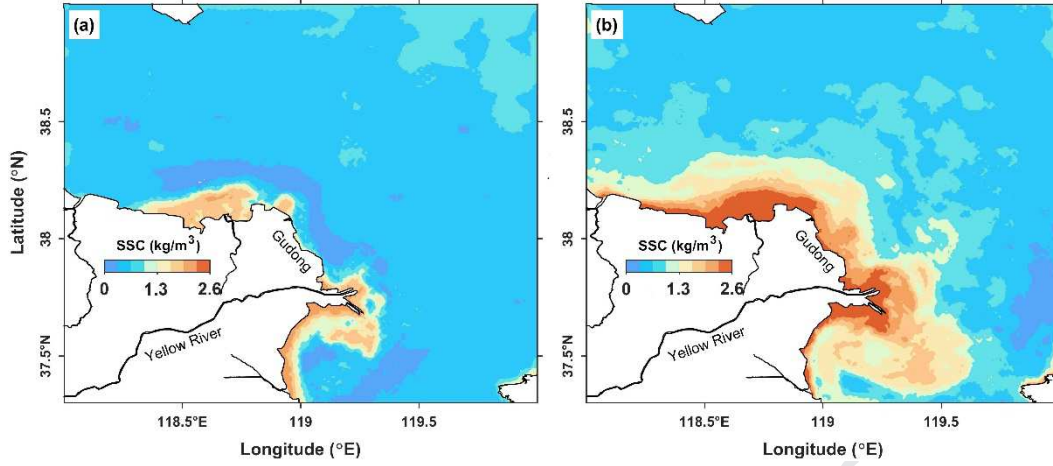
504

505 **Fig. 12.** The depth-averaged SSC: (a) in normal conditions; and (b) in storm conditions.
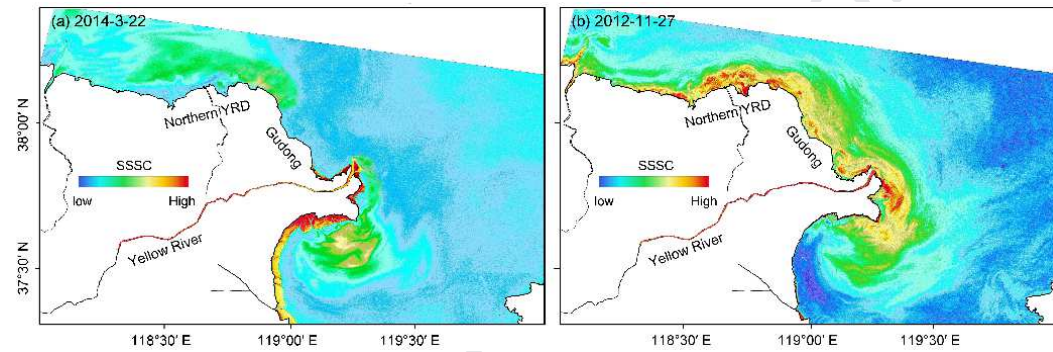
506

507 **Fig. 13.** Surface SSC (SSSC) retrieved from Landsat in the YRD region under: (a) in normal

508 condition; and (b) under strong wind conditions.
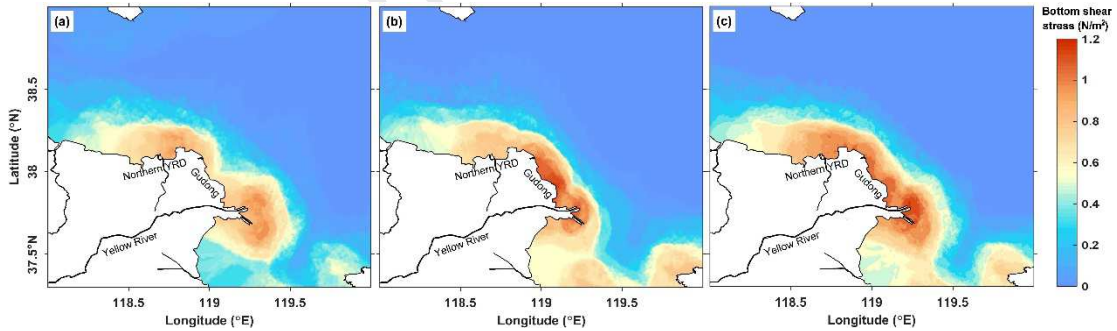
509

510 **Fig.14.** Bottom shear stress (units: N/m^2) in the littoral area of YRD: (a) current-induced; (b)

511 wave-induced; and (c) total.

512 *4.3.2 Sediment transport*

513   In this section, the sediment transport characteristics were analyzed by

514 calculating the residual transport of sediment (Tr_{sed}) through a unit width, which can

515 be defined as follows:

$$Tr_{sed} = \frac{1}{T} \int_0^T \int_{-H}^{\eta} \vec{V}(x,y,z,t) \cdot C(x,y,z,t) \mathrm{d}t \qquad (12)$$

29

516   where η is the surface elevation, H is the still water depth, and $\vec{V}$ is the horizontal

517   velocity vector, C is the sediment concentration, and T is the time period. As shown in

518   Fig. 7, the whole process of the repeated storm lasted for nearly 50 hours. During the

519   whole process, a wind turn occurred, forming two strong wind periods with different

520   directions, i.e. the northeasterly wind period (NEP) and the northwesterly wind period

521   (NWP). The dividing time of these two periods was approximately the middle time of

522   the whole storm process, thus we can take 25 h as T to calculate Tr_{sed} of these two

523   periods. The average SSC and residual of sediment transport rate are shown in Fig.

524   15.

525   From Fig. 15, we can see that the NEP was the growth and duration of storm

526   process with larger average wind speed, while the NWP showed a downward trend.

527   Therefore, the NEP appeared a larger maximum value of than the NWP. Although the

528   wind speed was weakening as a whole during the NWP, there was also a process of

529   wind acceleration with a maximum wind speed of 18.0 m/s. During the process of

530   offshore and southward transportation of sediment, a large amount of suspended

531   sediment diffuses to the sea and Laizhou Bay. Therefore, during the NWP the area of

532   high SSC was more widely distributed, and the area larger than 1.5 kg/m^3 increased

533   by nearly 50% compared with the NEP.
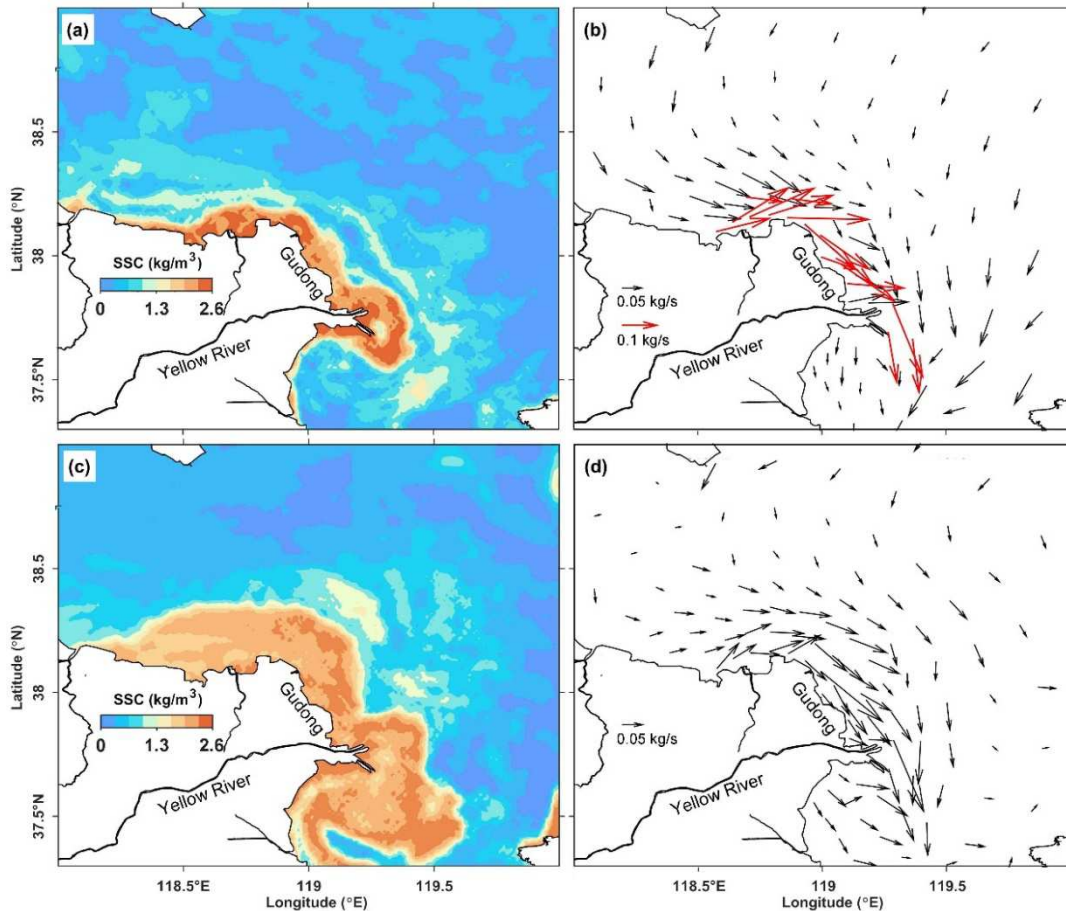
534
535 **Fig. 15.** The sediment transport features: (a) the suspended sediment concentrations and (b)
536 residual sediment mass transport during northeasterly wind; (c) the suspended sediment
537 concentrations and (d) residual sediment mass transport during northwesterly wind.

538 During the NEP, the residual transport of sediment increased with the decrease of

539 water depth. The larger value appeared off the Gudong coast, with the value of 0.23

540 kg/s. Although the residual transport of sediment during the NWP was less than that

541 during the NEP, it also showed a trend of increasing with the decrease of water depth,

542 with a high value of more than 0.18 kg/s off the Gudong coast and river mouth. The

543 directions of sediment transport were similar during these two periods, and basically

544 consistent with the direction of water transport. The main difference of them occurred

545 in the deep area, but the rates were mostly less than 0.05 kg/s. In both periods, the

546 sediment was transported offshore and southward as a whole. Specifically, the

547 sediment along the northern YRD coast was mainly transported eastward. After

548   arriving at the Gudong coast, sediment was transported southeast, and continued to

549   transport to the central area of the Laizhou Bay after passing the river mouth.

550   Different from the offshore transport in the littoral area of YRD during storm

551   surge, the sediment is transported landward by the storm surge in the Yangtze River

552   submerged delta (Dai et al. 2015). Coastal geometry may account for this difference:

553   compared with Bohai Bay and Laizhou Bay, the main coastline of the Yellow River

554   Delta protrude toward the sea, which makes the storm energy easier to gather in its

555   near shore; while the Yangtze River Delta is characterized as a channel-shoal system

556   with multiple outlets and shallow shoals, and the sediment can be transported to the

557   shore along the channel. Similarly, along the Ebro Delta coast (Spain) whose

558   geometry is cusp, researchers found that future trends in sea level rise produce

559   exacerbated cross-shore sediment transport by storm forcing (Grases et al. 2020).

560   **4.4 Seabed erosion**

561   Having identified the main directions and magnitudes of sediment transport, the

562   resulting morphological changes due to the storm are investigated. The final

563   bathymetric changes, obtained from Runs 1 and 2, are shown in Fig. 16a and Fig. 16b,

564   respectively. Positive values hereafter represent accretion and negative values

565   represent erosion. It can be seen that in most parts of the littoral area the bed level

566   changed within the confines of -0.05 m to 0.05 m in normal conditions (Fig. 16a). The

567   seabed erosion off Gudong was also slight due to its insignificant sediment transport.

568   Whereas in storm conditions, the changing hydrodynamics and sediment transport

569   induced significant nearshore erosion. Fig. 16b shows that the seabed erosion of the

570   Gudong and the northern YRD reached 0.1 m to 0.15 m, even more than 0.2 m near

571   the dike area. While, the main siltation occurred in the central area of Laizhou Bay.

572   Overall, the area (off the YRD, 118°E -120°E, 37.3°N -38°N) of seabed erosion in

573   storm conditions was 362.67 km^2, nearly 3 times as large as that in normal conditions,

574   and the erosion volume is 0.0543 km^3, about 20 times as large as that in normal

575   conditions. Therefore, the seabed erosion caused by the changes of hydrodynamics

576   and sediment transport under storm surge is an important factor in the coastal seabed

577   erosion of the YRD.

578   In order to explore the seabed changes after the storm, the bathymetric changes

579   during the recovery period after the storm were calculated. The time range of recovery

580   period was determined according to the wind speed and direction observed in P2 site.

581   As shown in Fig. 17, the end of this strong wind at 3:00 on April 15, indicating the

582   recovery period began at this time. At the time of 22:00 on April 18, strong wind

583   occurred again, indicating the recovery period began at this time and it lasted totaling

584   91 hours. Similar to the SSC calculated in the normal conditions in experiment 1, the

585   SSC off the north YRD and the active river mouth area was about 1.5 kg/m^3, while in

586   other areas it was less than 0.5 kg/m^3 (Fig. 18a). The residual transport of sediment

587   through a unit width was also similar to that calculated in Experiment 1 in light wind

588   conditions. There was no strong deposition or erosion area, and it was basically in the

589   equilibrium state during recovery period (Fig.18b). Along Guong coast, which had

590   been severely eroded during storm period, the bathymetry did not change significantly.

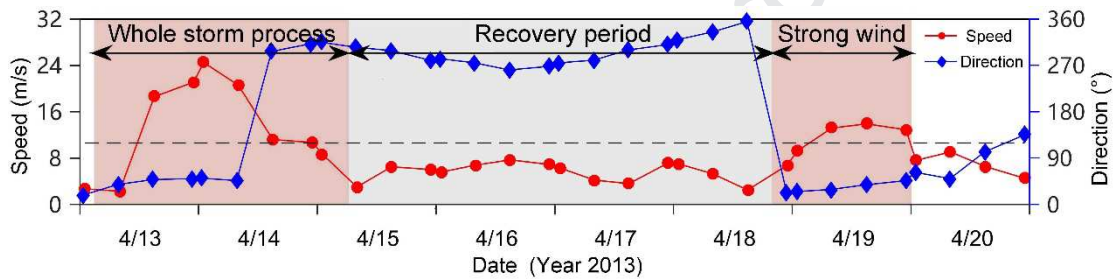591   It can be seen that it was difficult to recover the seabed erosion in the short term after

33

592   the storm, due to the insignificant sediment transport and deposition.
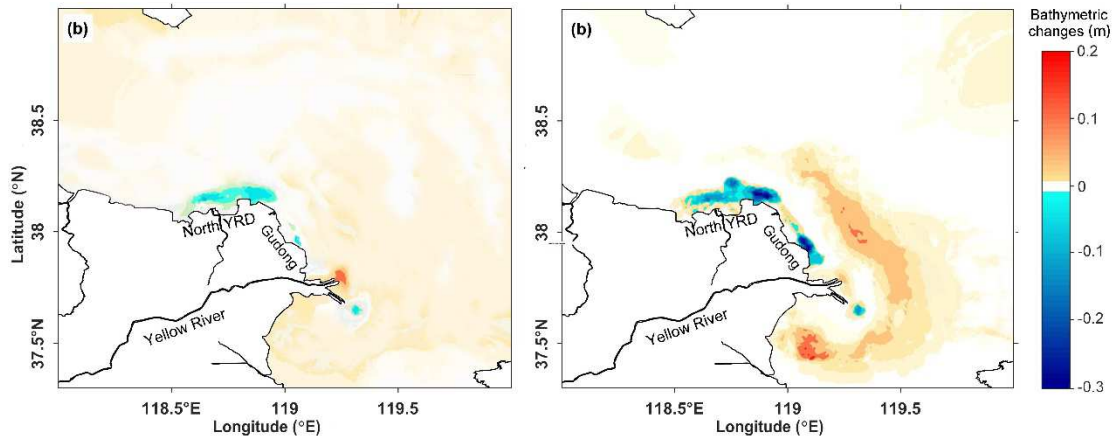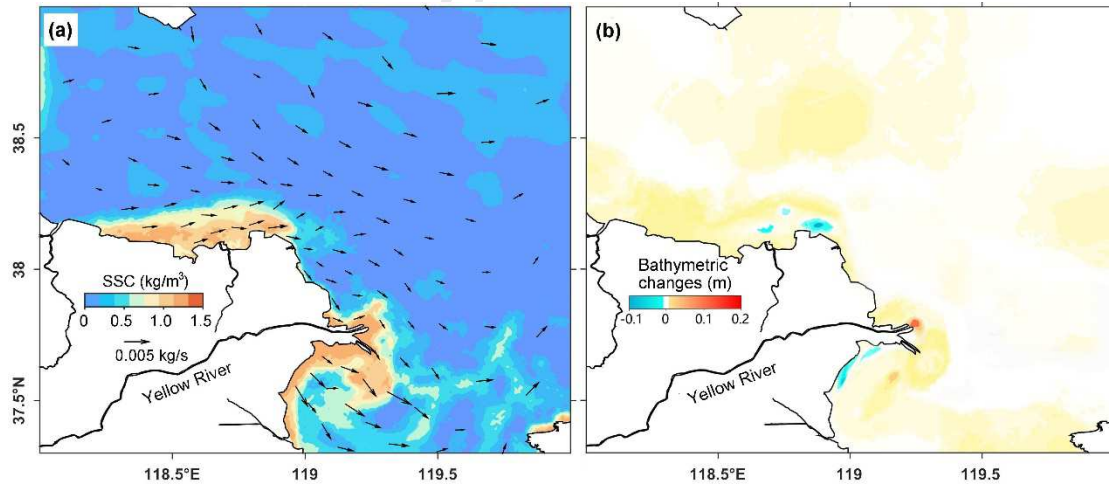

594 **Fig. 16.** Computed bathymetric changes (a) in normal conditions, and (b) in storm conditions.
595 Positive values represent accretion and negative values represent erosion.

597 **Fig. 17.** The changes of wind speed and direction during and after the storm.

599 **Fig. 18.** (a) Suspended sediment concentrations and residual sediment mass transport after the
600 storm; (b) erosion and accretion pattern after the storm.

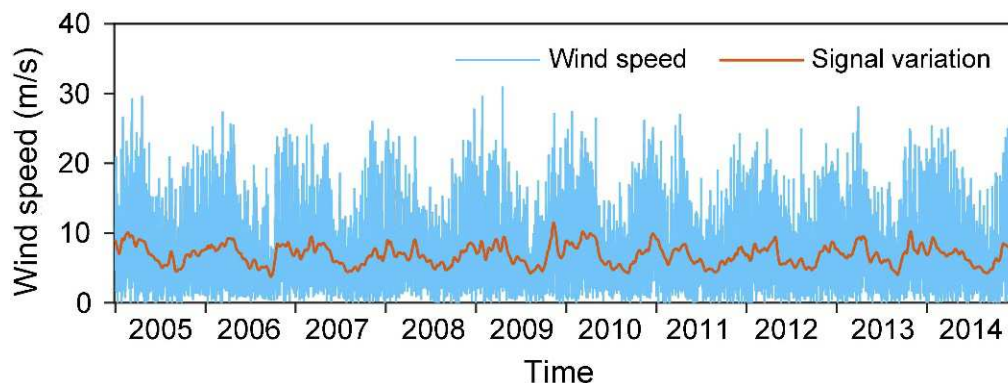601 **4.5 Frequency of strong wind**

602   The northern YRD and the Gudong coast are abandoned delta lobes, which

603 underwent erosion after the river channel shifted southward. Despite of the coastal

604 defenses (dikes) being built, the overall coastal area continued to be in the state of

34

605   erosion and coastal managers were obliged to build protection works constantly, for

606   example the pipe pile projects outside the destroyed dikes in 2004 and in 2016.

607   Previous studies attributed the long term erosion to the avulsion of Yellow River and

608   subsequent lack of sediment supply (Li et al., 2000; Xing et al., 2016), while this short

609   timescale event hardly explain the long-term eroded states.

610   Although the winter storm surge is an extreme event, the storm-induced coast

611   erosion plays an important role in the coastal geomorphological changes of the YRD.

612   On the one hand, the effects of a storm give a distinguished interpretation for the

613   seabed erosion, and on the other hand, storms occur at a higher frequency. Based on

614   the hourly wind field data of P2 site from 2005 to 2014, the time series variation

615   process of wind speed is analyzed. As shown in Fig. 19, the wind speed series has

616   obvious seasonal variation characteristics. In winter and spring, the wind speeds are

617   larger, while in summer, the wind speed is smaller. From the monthly scale change

618   process of wind speed, the average probability of strong wind (speed more than 10.8

619   m/s) for 7 consecutive months from October to May of next year is 10.28%, the

620   maximum is 22.14%, which appears in February of 2009.

621

622   **Fig. 19.** Time series of observed wind speed and the signal variations in a monthly scale.

623   Using the ECMWF wind data, the frequency and interval time of strong wind in

624 autumn-winter-spring (October 15 to April 15 of next year) since 1976 can be

625 calculated. The results are shown in Fig. 20. Statistics show that the average number

626 of strong wind occurred 39 times per period, 31 times at least, from October 1981 to

627 May 1982, and 48 times at most, from October 2016 to May 2017. Since 1976, the

628 number of strong winds has fluctuated slightly upward, while the average time

629 interval of strong wind has fluctuated slightly downward. Thus, in the past 40 years,

630 the YRD has seen more frequent strong winds. This fact indicates that the erosion

631 state is mainly due to the accumulative effect of scour during storms, not merely

632 attributable to the frequent avulsion.
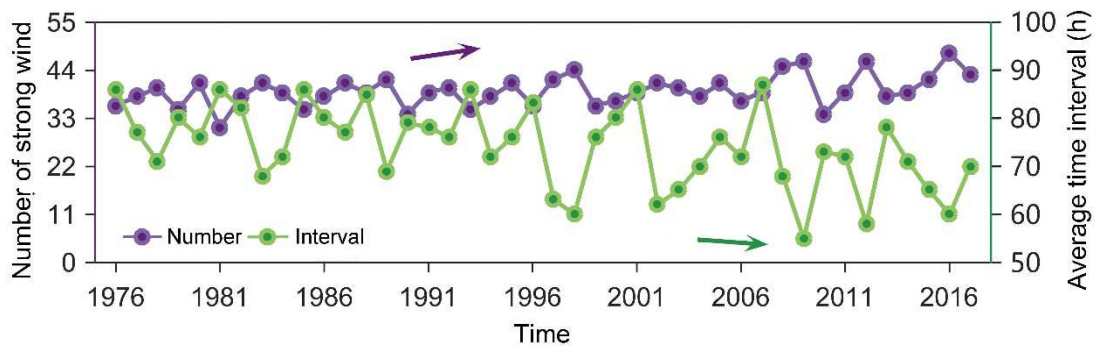
633

634 **Fig. 20.** Variation of the number of strong winds in autumn-winter-spring and the mean time
635 between two strong winds since 1976.

636 ## 5   Conclusions

637   In this study, the effect of storms on the hydrodynamics and sediment transport

638 off the YRD were examined using a coupled modelling system including tides, waves,

639 and sediment processes. Verifications of flow field, wave heights, tides, sediment

640 concentrations demonstrated that the model can reproduce the hydrodynamic and

641 sediment processes and indicated storm erosion occurring in nearshore zones of the

642 northern YRD and Gudong.

643   The results of numerical experiments show that the interactions between the tide

644   and wind-driven current during a storm period strengthen the residual currents and

645   weaken the tidal shear front in the shallow areas. In addition to hydrodynamic

646   changes, the strong northerly wind used in this numerical model causes the maximum

647   wave heights of more than 2 m appearing at the Gudong coast. Under the influence of

648   changing hydrodynamics during the storm, resuspension and sediment transport

649   occurs, which leads to higher sediment concentration, with the maximum SSC

650   exceeding 2.5 kg/m^3 nearshore the northern YRD. The local resuspension due to

651   greater wave-induced bottom stress promotes the sediment plume to shift to the

652   Gudong coast. Besides, the sediment transported offshore and southward. The

653   dynamic and sediment transport changes under storm conditions caused significant

654   changes in seabed erosion and siltation. The area of seabed erosion area was nearly

655   three times as large as that under normal conditions, and the erosion volume was

656   nearly 20 times as large as that under normal conditions. No significant recovery after

657   a storm and frequent strong winds have an accumulative effect on the seabed erosion.

658   The results from this study improve our understanding of the formation mechanism of

659   the eroded coast in the YRD: the accumulated storm erosion is more likely to

660   dominate the long-term erosive coastal states, not just the frequent avulsion and of

661   Yellow River and subsequent discontinuity of sediment supply.

677 **References**

678   Allen, J.I., Somerfield, P.J., Gilbert, F.J., 2007. Quantifying uncertainty in high-resolution coupled
679   hydrodynamic-ecosystem models. Journal of Marine Systems 64, 3-14.

680   Anthony, E.J., 2015. Wave influence in the construction, shaping and destruction of river deltas: A
681   review. Marine Geology 361, 53-78.

682   Becker, M., Papa, F., Karpytchev, M., Delebecque, C., Krien, Y., Khan, J.U., Ballu, V., Durand, F.,
683   Cozannet, G.L., Islam, A.K.M.S., Calmant, S., Shum, C.K., 2020. Water level changes,
684   subsidence, and sea level rise in the Ganges-Brahmaputra-Meghna delta. PNAS 117(4),
685   1867-1876.

686   Beihai Branch of State Oceanic Administration People's Republic of China. The northern China
687   Marine Disasters Bulletin (2013) [EB/OL] http://ncs.mnr.gov.cn/. 2014-04-01.

688   Bi, N.S., Wang, H.J., Yang, Z.S., 2014. Recent changes in the erosion-accretion patterns of the
689   active Huanghe (Yellow River) delta lobe caused by human activities. Continental Shelf

690   Research 90: 70-78.

691   Bian, S.H., Hu, Z., Liu, J., Zhu, Z., 2016. Sediment suspension and the dynamic mechanism

692   during storms in the Yellow River Delta. Environmental Monitoring & Assessment, 189: 3.

693   Bjarnadottir, S. 2011. Social vulnerability index for coastal communities at risk to hurricane

694   hazard and a changing climate. Natural Hazards 59, 1055-1075.

695   Blum, M.D., Roberts, H.H., 2009. Drowning of the Mississippi Delta due to insufficient sediment

696   supply and global sea-level rise. Nature Geoscience 2, 488-491.

697   Boudet, L.F., Sabatier, F., Radakovitch, O., 2017. Modelling of sediment transport pattern in the

698   mouth of the Rhone delta: Role of storm and food events. Estuarine, Coastal and Shelf

699   Science 198, 568-582.

700   Brown, J.M., Ciavola, P., Masselink, G., Mccall, R., Plater, A.J., 2016. Preface: monitoring and

701   modelling to guide coastal adaptation to extreme storm events in a changing climate. Natural

702   Hazards & Earth System Sciences 16, 463-467.

703   Cao, Z.D., Lou, A.G., 2011. A three dimensional numerical simulation of the wind-driven

704   circulation during winter in the Bohai Sea by FVCOM (in Chinese with English abstract).

705   Periodical of Ocean University of China, 6787: 183-194

706   Chen, G., Niu, Y., Wen, S., Bao, C., Wu, B., Zhang, R., Gu, H., 1992. Marine Atlas of Bohai Sea,

707   Yellow Sea, East China Sea: Hydrology. China Ocean Press, Beijing. p.523.

708   Chen, S., Zhang, G., Chen, X., 2006. Coastal erosion feature and mechanism at Feiyantan in the

709   Yellow River delta. Marine Science Bulletin 8, 11-20.

710   Dai, Z.J., Fagherazzi, S., Mei, X.F., Gao, J.J., 2016. Decline in suspended sediment concentration

711   delivered by the Changjiang (Yangtze) River into the East China Sea between 1956 and 2013.

712   Geomorphology 268, 123-132.

713   Dou, G.R., 1999. Incipient motion of coarse and Fine sediment (in Chinese, with English abstract).

714   Journal of Sediment Research 6, 1-9.

715   Edmonds, D.A., Slingerland, R.L., 2010. Significant effect of sediment cohesion on delta

716   morphology. Nature Geoscience 3, 105-109.

717   Fan, Y.S., Chen, S.L,. Zhao, B., Pan, S., Jiang, C., Ji, H.Y., 2018. Shoreline dynamics of the active

718   Yellow River delta since the implementation of Water-Sediment Regulation Scheme: a

719   remote-sensing and statistics-based approach. Estuarine, Coastal and Shelf Science 200,

720   406-419.

721   Florin, I.Z., Florin, T., Nikolay, N.V., Alfred, V.S., 2017. Storm climate on the Danube delta coast:

722   evidence of recent storminess change and links with large-scale teleconnection patterns.

723   Natural Hazards 87, 1-23.

724   Goff, J.A., Allison, M.A., Gulick, S.P.S., 2010. Offshore transport of sediment during cyclonic

725   storms: Hurricane Ike (2008), Texas Gulf Coast, USA. Geology 38, 351–354.

726   Gong, W., Jia, L., Shen, J., Liu, J.T., 2014. Sediment transport in response to changes in river

727   discharge and tidal mixing in a funnel-shaped micro-tidal estuary. Continental Shelf Research

728   76, 89-107.

729   Grant, W.D., Madsen, O.S., 1979. Combined wave and current interaction with a rough bottom.

730   Journal of Geophysical Research 84, 1797-1808.

731   Grases, A., Gracia, V., García-León, M., Jue, L.Y., Sierra, J.P., 2020. Coastal flooding and erosion

732   under a changing climate: Implications at a low-lying coast (Ebro Delta). Water 12, 346.

733   Hao, Y., Le, K.T., Liu, X.Q., 2010. A numerical prediction of the tidal characteristics in 2010 of

734   Yellow River Delta (in Chinese, with English abstract). Chinese Marine Science 24, 43-46.

735   Huang, D., 1995. Modeling Studies of Barotropic and Baroclinic Dynamics in the Bohai Sea.

736   Ph.D Thesis. Hamburg, Germany: Hamburg University.

737   Huang, D.J., Chen, Z.Y., Su, J.L., 1996. Application of three-dimensional shelf sea model in the

738   Bohai Sea: I. tidal current, wind-driven current and their interaction (in Chinese, with English

739   abstract). Aeta Oceanologia Sinica 18, 1-15.

740   Jiang, C., Pan, S., Chen, S.L., 2017. Recent morphological changes of the Yellow River (Huanghe)

741   submerged delta: causes and environmental implications. Geomorphology 293, 93-107.

742   Kong, D., Miao, C., Borthwick, A.G.L., Duan, Q.Y., Liu, H., Sun, Q.H., Ye, A.Z., Di, Z.H., Gong

743   W., 2015. Evolution of the Yellow River delta and its relationship with runoff and sediment

744   load from 1983 to 2011. Journal of Hydrology 520, 157-167.

745   Uehara, K., Pramot, S., Yoshiki, S., Thanawat, J., 2010. Erosion and accretion processes in a

746   muddy dissipative coast, the Chao Phraya River delta, Thailand. Earth Surface Processes and

747   Landforms 35(14), 1701-1711.

748   Kuenzer, C., Ottinger, M., Liu, G.H., Sun, B., Baumhauer, R., Dech, S., 2014. Earth observation

749   based coastal zone monitoring of the Yellow River delta: dynamics in China's second largest

oil producing region observed over four decades. Applied Geography 55, 92-107.

Li, G.X., Cheng, G., Wei, H., Pan, W., Ren, Y., Ding, D., Zhou, Y., Zhao, J., 1994. Tidal shear front off modern Yellow River mouth. Chinese Science Bulletin 39, 928–932.

Li, G.X., Zhuang, K., Wei, H., 2000. Sedimentation in the Yellow River delta. Part III. Seabed erosion and diapirism in the abandoned subaqueous delta lobe. Marine Geology 168, 129-144.

Li, Y., Tian, L.Z., Pei, Y.D., Wang, F., Wang, H., 2016. Numerical simulation of storm surge inundation in the west zone of Bohai Bay. Geological Bulletin of China 35(10), 1638-1645.

Liu, F., Chen, H., Cai, H., Luo, X., Ou, S., Yang, Q., 2017. Impacts of ENSO on multi-scale variations in sediment discharge from the Pearl River to the South China Sea. Geomorphology 293, 24-36.

Liu, F., Xie, R., Luo, X., Yang, L., Cai, H., Yang, Q., 2019. Stepwise adjustment of deltaic channels in response to human interventions and its hydrological implications for sustainable water managements in the Pearl River Delta, China. Journal of Hydrology 573, 194-206.

Liang, B.C., Li, H.J., 2008. Bottom shear stress under wave-current interaction. Journal of Hydrodynamics Series B 20, 88-95.

Lu, J., Qiao, F.L., Wang, X.H., Wang, Y.G., Teng, Y., Xia, C.S., 2011. A numerical study of transport dynamics and seasonal variability of the Yellow River sediment in the Bohai and Yellow Seas. Estuarine Coastal and Shelf Science 95, 39-51

Luo, Z., Zhu, J., Wu, H., Li, X., 2017. Dynamics of the sediment plume over the Yangtze Bank in the Yellow and East China Seas. Journal of Geophysical Research Oceans 122, 10073-10090.

Lv, X., Yuan, D., Ma, X., Tao, J., 2014. Wave characteristics analysis in Bohai Sea based on ECMWF wind field. Ocean Engineering 91, 159-171.

Martin, J., Sheets, B., Paola, C., Hoyal, D., 2009. Influence of steady base-level rise on channel mobility, shoreline migration, and scaling properties of a cohesive experimental delta. Journal of Geophysical Research Earth Surface 114, F03017.

Milly, P.C., Wetherald, R.T., Dunne, K.A., Delworth, T.L., 2002. Increasing risk of great floods in a changing climate. Nature 415, 514-517.

Murray, N.J., Phinn, S.R., DeWitt, M., 2019. The global distribution and trajectory of tidal flats. Nature 565, 222-225.

780 Nichollsm R.J., Cazenavem, A., 2010. Sea-level rise and its impact on coastal zones. Science 328,

781   1517.

782 Pelling, H.E., Uehara, K., Green, J.A.M., 2013. The impact of rapid coastline changes and sea

783   level rise on the tides in the Bohai Sea, China. Journal of Geophysical Research: Oceans 118,

784   3462-3472.

785 Qi, S., Liu, H., 2017. Natural and anthropogenic hazards in the Yellow River Delta, China. Natural

786   Hazards 85, 1-5

787 Qiao, L.L., Bao, X.W., Wu, D.X., Wang, X.H., 2008. Numerical study of generation of the tidal

788   shear front off the Yellow River mouth. Continental Shelf Research 28, 1782-1790.

789 Quan, Y.Z., 2014. Numerical simulation of sediment movement and its dynamic mechanism in a

790   strong wind processed of northern sea of the Yellow River Delta. Doctoral Dissertation.

791   Qingdao, China: Ocean University of China.

792 Ralston, D.K., Geyer, R., Lerczak, J.A., 2010. Structure, variability, and salt flux in a strongly

793   forced salt wedge estuary. Journal of Geophysical Research: Oceans 115, C06005.

794 Ralston, D.K., Warner, J.C., Geyer, W.R., Wall, G.R., 2013. Sediment transport due to extreme

795   events: the Hudson River estuary after tropical storms Irene and Lee. Geophysical Research

796   Letters 40, 5451-5455.

797 Reitz, M.D., Jerolmackm, D.J., 2012. Experimental alluvial fan evolution: Channel dynamics,

798   slope controls, and shoreline growth. Journal of Geophysical Research: Earth Surface 117,

799   F02021.

800 Ren, R., Chen, S.L., Dong, P., Liu, F., 2012. Spatial and temporal variations in grain size of

801   surface sediments in the littoral area of Yellow River delta. Journal of Coastal Research 28,

802   44-53.

803 Shi, W., Wang, M., Jiang, L., 2011. Spring-neap tidal effects on satellite ocean color observations

804   in the Bohai Sea, Yellow Sea, and East China Sea. Journal of Geophysical Research 116:

805   C12032.

806 Signell, R.P., Beardsley, R.C., Graber, H.C., Capotondi, A., 1990. Effect of wave-current

807   interaction on wind-driven circulation in narrow, shallow embayments. Journal of

808   Geophysical Research 95, 9671-9678.

809 Syvitski, J.P.M, Kettner, A., 2011. Sediment flux and the Anthropocene. Philosophical

810   Transactions of the Royal Society A: Mathematical, Physical and Engineering Sciences 369,

811   957-975.

812   Tessler, Z.D., Vorosmarty, C.J., Grossberg, M., et al., 2015. Profiling risk and sustainability in

813   coastal deltas of the world. Science 349, 638-643.

814   Vaz, N., Dias, J.M., 2014. Residual currents and transport pathways in the Tagus estuary, Portugal:

815   the role of freshwater discharge and wind. Journal of Coastal Research 70, 610-615.

816   Van Rijn, L.C., 1993. Principles of sediment transport in river, estuaries and coastal seas. AQUA

817   Publications, the Netherlands, p.535.

818   Wang, H., Bi, N., Saito, Y., Wang, Y., Sun, X., Zhang, J., Yang, Z., 2010. Recent changes in

819   sediment delivery by the Huanghe (Yellow River) to the sea: causes and environmental

820   implications in its estuary. Journal of Hydrology 391, 302-313.

821   Wang, H., Saito, Y., Zhang, Y., Bi, N., Sun, X., Yang, Z., 2011. Recent changes of sediment flux to

822   the western Pacific Ocean from major rivers in East and Southeast Asia. Earth-Science

823   Reviews 108, 80-100.

824   Wang, H., Wang, A., Bi, N., Zeng, X., Xiao, H., 2014. Seasonal distribution of suspended

825   sediment in the Bohai Sea, China. Continental Shelf Research 90, 17-32.

826   Wang, H., Yang, Z., Li, Y., Guo, Z., Sun, X., Wang, Y., 2007. Dispersal pattern of suspended

827   sediment in the shear frontal zone off the Huanghe (Yellow River) mouth. Continental Shelf

828   Research 27, 854-871.

829   Wang, N., Li, G., Qiao, L., Shi, J., Dong, P., Xu, J., Ma, Y., 2017. Long-term evolution in the

830   location, propagation, and magnitude of the tidal shear front off the Yellow River mouth.

831   Continental Shelf Research 137, 1-12.

832   Warner, J.C., Sherwood, C.R., Signell, R.P., Harris, C.K., Arango, H.G., 2008. Development of a

833   three-dimensional, regional, coupled wave, current, and sediment-transport model.

834   Computers & Geosciences 34, 1284-1306.

835   Winterwerp, J.C., Maa, J., Sanford, L., Schoellhamer, D., 2007. On the sedimentation rate of

836   cohesive sediment. In: Estuarine and Coastal Fine Sediments Dynamics INTERCOH 2003.

837   Elsevier, p. 209-226.

838   Wolters, M.L., Kuenzer, C., 2015. Vulnerability assessments of coastal river deltas-categorization

839   and review. Journal of Coastal Conservation 19, 345-368.

840　Wu, X., Bi, N., Xu, J., Nittrouer, J.A., Yang, Z., Saito, Y., Wang, H., 2017. Stepwise
841　　morphological evolution of the active Yellow River (Huanghe) delta lobe (1976–2013):
842　　dominant roles of riverine discharge and sediment grain size. Geomorphology 292, 115-127.

843　Wu, X., Bi, N., Yuan, P., Li, S., Wang, H., 2015. Sediment dispersal and accumulation off the
844　　present Huanghe (Yellow River) delta as impacted by the Water-Sediment Regulation
845　　Scheme. Continental Shelf Research 111, 126-138.

846　Xing, F., Wang, Y.P., Wang, H.V. 2012. Tidal hydrodynamics and fine-grained sediment transport
847　　on the radial sand ridge system in the southern Yellow Sea. Marine Geology 291-294,
848　　192-210.

849　Xing, G., Wang, H., Yang, Z., Bi, N., 2016. Spatial and temporal variation in erosion and
850　　accumulation of the subaqueous Yellow River delta (1976–2004). Journal of Coastal
851　　Research 74, 32-47.

852　Xu, C., Gu, S., Liu, Z., Zhang, N., Yu, L., 2016. Characteristics of the river mouth bar in the past
853　　14 years of the Yellow River Water-Sediment Regulation (in Chinese, with English abstract).
854　　Yellow River 38, 69-73.

855　Yang, S., Milliman, J.D., Li, P., Xu, K., 2011a. 50,000 dams later: erosion of the Yangtze River
856　　and its delta. Global and Planetary Change 75, 14-20.

857　Yang, Z., Ji, Y., Bi, N., Lei, K., Wang, H., 2011b. Sediment transport off the Huanghe (Yellow
858　　River) delta and in the adjacent Bohai Sea in winter and seasonal comparison. Estuarine
859　　Coastal and Shelf Science 93, 173-181.

860　Ying, M., Li, J.F., Chen, S.L., Dai, Z.J., 2008. Dynamics characteristics and topographic profile
861　　shaping process of Feiyan Shoal at the Yellow River delta. Marine Science Bulletin 10,
862　　74-88.

863　Yuan, D., Zhu, J., Li, C., Hu, D., 2008. Cross-shelf circulation in the Yellow and East China Seas
864　　indicated by MODIS satellite observations. Journal of Marine Systems 70, 134-149.

865　Zhang, M., Dong, Q., Cui, T., Xue, C., Zhang, S., 2014. Suspended sediment monitoring and
866　　assessment for Yellow River estuary from Landsat TM and ETM+ imagery. Remote Sensing
867　　of Environment 146, 136-147.

868　Zhang, Y., 2011. Coastal environmental monitoring using remotely sensed data and GIS
869　　techniques in the modern Yellow River delta, China. Environmental Monitoring &

44

870   Assessment 179, 15-29.

Highlights

- Storm-induced energetic hydrodynamic forces intensify sediment resuspension and dispersal significantly.

- Wave-induced bottom stress promotes sediment plume and enhances local resuspension.

- Storms increase suspended sediment concentration and offshore sediment transport.

- Storm-induced accumulative effect on seabed scour tends to cause long-term erosion.

Conflict of interest

The authors declared that they have no conflicts of interest to this work. We declare that we do not have any commercial or associative interest that represents a conflict of interest in connection with the work submitted.